Hindawi
Mathematical Problems in Engineering
Volume 2018, Article ID 6768947, 18 pages
https://doi.org/10.1155/2018/6768947

Research Article

Kinematics Performance and Dynamics Analysis of a Novel Parallel Perfusion Manipulator with Passive Link

Hui Yang,[1] Hairong Fang ,[1,2] Yuefa Fang,[1,2] and Haibo Qu[1]

[1] *Robotics Research Center, School of Mechanical Electronic and Control Engineering, Beijing Jiaotong University, Beijing 100044, China*
[2] *Key Laboratory of Vehicle Advanced Manufacturing, Measuring and Control Technology, Beijing Jiaotong University, Ministry of Education, Beijing, China*

Correspondence should be addressed to Hairong Fang; hrfang@bjtu.edu.cn

Received 9 August 2018; Revised 3 October 2018; Accepted 21 October 2018; Published 25 November 2018

Academic Editor: Jorge Pomares

In order to solve the problem of the honeycombs perfusion in the thermal protection system of the spacecraft, this paper presents a novel parallel perfusion manipulator with one translational and two rotational (1T2R) degrees of freedom (DOFs), which can be used to construct a 5-DOF hybrid perfusion system for the perfusion of the honeycombs. The proposed 3$\underline{P}$SS&PU parallel perfusion manipulator is mainly utilized as the main body of the hybrid perfusion system. The inverse kinematics and the Jacobian matrix of the proposed parallel manipulator are obtained. The analysis of kinematics performance for the proposed parallel manipulator including workspace, singularity, dexterity, and stiffness is conducted. Based on the virtual work principle and the link Jacobian matrix, the dynamic model of the parallel perfusion manipulator is carried out. With reference to dynamic equations, the relationship between the driving force and the mechanism parameters can be derived. In order to verify the correctness of the kinematics and dynamics model, the comparison of theoretical and simulation curves of the motion parameters related to the driving sliders is performed. Corresponding analyses illustrate that the proposed parallel perfusion possesses good kinematics performance and could satisfy the perfusion requirements of the honeycombs. The correctness of the established kinematics and dynamics models is proved, which has great significance for the experimental research of the perfusion system.

1. Introduction

During the rise and reentry of the spacecraft, the crew module of spacecraft will suffer from a large aerodynamic heating effect. Therefore, thermal protection system is needed to ensure the safety of the pilot and the normal operation of the equipment [1–3]. At present, the structure of spacecraft thermal protection layer usually adopts hexagonal honeycomb structure, and then these honeycombs are spliced together and evenly spread on the surface of spherical crown. In order to achieve the effect of thermal protection, it needs to perfuse the heat-resistant material into the honeycomb structure [4]. However, due to the large size of spherical surface structure, the perfusion of heat-resistant material becomes the main problem. At present, it mainly adopts manual perfusion, which will inevitably require more manpower to complete the perfusion. Accordingly, it is necessary to introduce perfusion manipulator into the perfusion system.

In the perfusion system, all the perfusion of the honeycombs is conducted based on the detection system. Due to the large size of the spherical crown surface, the perfusion object will be divided into subregion for processing. First, according to the detection system's identification, the position of the task honeycombs can be identified. Then, through the rotation of the spherical crown worktable and the motion of the parallel perfusion manipulator, the perfusion of the task honeycombs can be accomplished. When the perfusion of the identified task honeycombs is completed, the detection system will conduct the identification of the next group of honeycombs. In the article, the design and analysis of the perfusion manipulator are the focus of our research.

As we all know, the traditional serial manipulator has the advantage of large workspace and the disadvantage of low stiffness, while the parallel manipulator with closed kinematic chain has some advantages compared with the serial manipulator, such as high structural rigidity, high dynamic

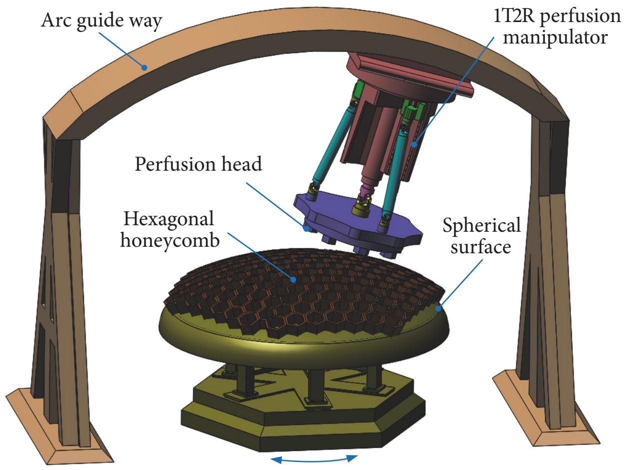

Figure 1: 3D model of the hybrid perfusion system.

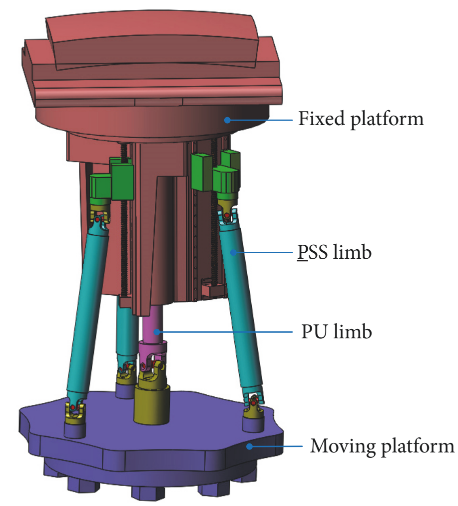

Figure 2: CAD model of the 1T2R parallel manipulator.

performance, high accuracy, and low moving inertia [5–9]. For such a reason, parallel manipulator has been extensively applied as flight simulator [10–12], machine tools [13–15], mobile machining module [16, 17], and high-speed pick-and-place robots [18–20]. However, the parallel manipulator also has the disadvantage of small workspace. For the perfusion system, the spherical structure is relatively large and the end of the moving platform needs to carry the heavy perfusion device, so it requires that the perfusion manipulator should have the characteristics of large workspace and high stiffness. However, due to the low stiffness of the serial manipulator and the small workspace of the parallel manipulator, all of them could hardly satisfy the perfusion requirements of the perfusion manipulator. Consequently, in order to solve these problems, hybrid manipulator with the advantages of serial manipulator and parallel manipulator is selected as the suitable perfusion manipulator.

Since the spherical crown surface can be seen as a complex free-form surface, the perfusion manipulator needs at least five DOFs (3T2R) in the process of the heat-resistant material perfusion. Generally, the 5-DOF hybrid manipulator can be achieved by adding a 2-DOF rotating head to the moving platform of a 3-DOF position adjustment manipulator, which are typically represented by Tricept [21, 22], Trivariant [23, 24], and Exechon machine tool [25, 26]. In addition, some scholars also constructed the 5-DOF hybrid manipulator by integrating a 3-DOF pose adjustment manipulator with two long guide rails, which are particularly taken as example as Sprint Z3 head [27, 28] and the machine tool [29, 30]. Motivated by this idea, this paper proposes a novel 1T2R parallel manipulator that can be used to construct 5-DOF hybrid perfusion system for the perfusion of the honeycombs in the thermal protection system of the spacecraft. For the 1T2R parallel manipulator, due to the introduction of the passive link, the stiffness of the proposed parallel manipulator has been improved. Moreover, since the idea that the moving platform size is larger than the fixed platform size, the singularity of the parallel manipulator is avoided effectively. And the structural of the proposed manipulator is simple, compact, symmetrical, and easy to control. Thus, because of the reasons mentioned above, the proposed parallel manipulator is selected for the perfusion of the honeycombs in the thermal protection system.

In this paper, the objective of the research mainly is aimed at the kinematics performance analysis and the establishment of the dynamics model for the proposed 1T2R parallel perfusion manipulator. The remainder of this article is given as follows. In Section 2, structure description of the proposed 1T2R parallel manipulator is represented. The analysis of kinematics and performance is conducted in Sections 3 and 4, respectively. In Section 5, based on the principle of virtual work, dynamic model of the proposed parallel manipulator is established. The simulation research is carried out by utilizing kinematics and dynamics model in Section 6. Conclusions are given in Section 7.

2. Architecture

2.1. Architecture Description. To satisfy the perfusion requirement of spherical surface, the perfusion manipulator should have at least five DOFs, which concludes three translational DOFs and two rotational DOFs. According to the requirements, a 5-DOF hybrid perfusion system is proposed, which is shown in Figure 1. The perfusion system consists of an arc guide way, a 1T2R parallel manipulator, and a honeycomb worktable. The 1T2R parallel manipulator can move along the arc guide way. The honeycomb worktable can rotate about its own axis, and the honeycomb structure is evenly spread in spherical surface. When the perfusion manipulator is at a certain position of the guide way, the perfusion head can achieve the perfusion of the honeycombs within the moving platform's reachable workspace. Through the rotation of the worktable and the movement of the parallel manipulator along the guide way, all the perfusion of honeycombs can be completed successfully.

Figure 2 indicates a CAD model of the 1T2R parallel manipulator, which consists of a fixed platform, three

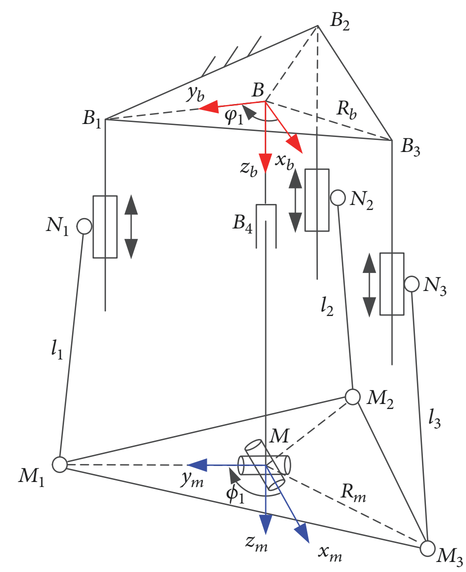

FIGURE 3: Kinematic diagram of the 1T2R parallel manipulator.

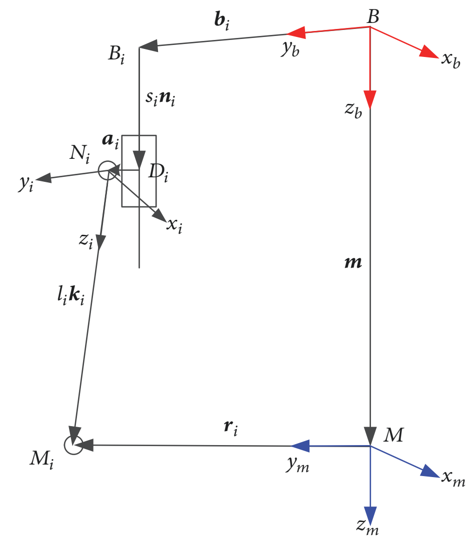

FIGURE 4: Kinematics of the ith PSS branch.

actuated PSS (P denotes the actuated joint) links, a moving platform, and the passive constraint link PU. Every PSS limb connects the fixed platform with perfusion platform by an active prismatic joint followed by two spherical joints. And every prismatic joint is driven by a servomotor. The passive limb contains a universal joint and a prismatic joint, which connects the perfusion platform with the fixed plate, successively. The existence of the PU limb will highly improve stiffness of the whole system.

2.2. Parameters Description. The schematic model of proposed manipulator in Figure 3 shows that it has two platforms: fixed platform labeled by $B_1B_2B_3$ and moving platform demonstrated by $M_1M_2M_3$. The three limbs are placed in 120 degree intervals on base platform. Links N_iM_i are attached to the moving platform by a spherical joint at M_i and to a slider by a spherical joint at N_i. The middle limb is established from the fixed platform to the perfusion platform, whose one end is attached to the base with a prismatic joint B_4 and the other end is attached to the end-effector platform by a universal joint. To facilitate the analysis, the fixed reference frame B-$x_by_bz_b$ is placed at the center of the base platform where y_b axis is along the direction of straight line BB_1. Similarly, the coordinate axes of moving frame are denoted by M-$x_my_mz_m$ in which y_m axis is along the direction of straight line MM_1. Parameter φ_i is the angle measured from x_b to BB_i and ϕ_i is the angle measured from x_m to MM_i. The length of the limb N_iM_i is denoted by l_i. The length of BB_i is demonstrated by R_b, and R_m represents the length of the line MM_i. The displacement of the driving joint is represented by s_i.

3. Kinematics Analysis

3.1. Inverse Kinematics. As shown in Figure 4, the relationship between the coordinate systems B-$x_by_bz_b$ and M-$x_my_mz_m$ can be described by the rotation matrix ${}^B\boldsymbol{R}_P$, which can be obtained by three continuous rotations of Euler angles α, β, and γ about the fixed x_b, y_b, and z_b axis, respectively. For the 1T2R parallel manipulator, the angle γ is zero. Thus, the rotation matrix from M-$x_my_mz_m$ coordinate system to B-$x_by_bz_b$ coordinate system can be expressed as

$$ {}^B\boldsymbol{R}_M = \mathrm{Rot}\left(y_b, \beta\right)\mathrm{Rot}\left(x_b, \alpha\right) = \begin{bmatrix} c\beta & s\beta s\alpha & s\beta c\alpha \\ 0 & c\alpha & -s\alpha \\ -s\beta & c\beta s\alpha & c\beta c\alpha \end{bmatrix} \quad (1) $$

where s and c correspond to the sine and cosine functions, respectively.

To facilitate the analysis, the local coordinate system N_i-$x_iy_iz_i$ of the ith PSS branch also has been established at the point N_i, and the z_i axis is along the direction of straight line N_iM_i. The system N_i-$x_iy_iz_i$ can be considered as two continuous rotations of angles κ_i and ψ_i about z_b axis and y_i' axis (rotated y_b axis), respectively. Consequently, the rotation matrix can be represented as

$$ \begin{aligned} {}^B\boldsymbol{R}_i &= \mathrm{Rot}\left(z_b, \kappa_i\right)\mathrm{Rot}\left(y_i', \psi_i\right) \\ &= \begin{bmatrix} c\kappa_i c\psi_i & -s\kappa_i & c\kappa_i s\psi_i \\ s\kappa_i c\psi_i & c\kappa_i & s\kappa_i s\psi_i \\ -s\psi_i & 0 & c\psi_i \end{bmatrix} \end{aligned} \quad (2) $$

According to Figure 4, the closed-loop vector equation of the ith link is given as follows:

$$ \boldsymbol{m} + \boldsymbol{r}_i = \boldsymbol{b}_i + s_i\boldsymbol{n}_i + \boldsymbol{a}_i + l_i\boldsymbol{k}_i \quad (3) $$

where $\boldsymbol{m}$ is the position vector of the moving platform described in B-$x_by_bz_b$ system, $\boldsymbol{r}_i = {}^B\boldsymbol{R}_M{}^m\boldsymbol{r}_i$, $\boldsymbol{r}_i$ and ${}^m\boldsymbol{r}_i$ represent the position vector of the straight line MM_i in B-$x_by_bz_b$ and M-$x_my_mz_m$ system, respectively, $\boldsymbol{b}_i$ is the position vector of the straight line OB_i in B-$x_by_bz_b$ system, while $\boldsymbol{n}_i$ and $\boldsymbol{k}_i$ denote the unit vector of the straight line B_iD_i and N_iM_i expressed in the coordinate system B-$x_by_bz_b$, respectively, s_i is the displacement of the prismatic joint for the ith PSS branch, and l_i is the length of the link N_iM_i. Therefore, the vectors mentioned above can be obtained as

$$\boldsymbol{m} = \begin{bmatrix} 0 \\ 0 \\ z_m \end{bmatrix};$$
$$^m\boldsymbol{r}_i = \begin{bmatrix} R_m c\phi_i \\ R_m s\phi_i \\ 0 \end{bmatrix};$$
$$\boldsymbol{b}_i = \begin{bmatrix} R_b c\varphi_i \\ R_b s\varphi_i \\ 0 \end{bmatrix}; \tag{4}$$
$$\boldsymbol{n}_i = \begin{bmatrix} 0 \\ 0 \\ 1 \end{bmatrix};$$
$$\boldsymbol{a}_i = \begin{bmatrix} d_1 c\varphi_i \\ d_1 s\varphi_i \\ 0 \end{bmatrix};$$

From 2), the unit vector $\boldsymbol{k}_i$ will be expressed as

$$\boldsymbol{k}_i = {}^B\boldsymbol{R}_i {}^i\boldsymbol{k}_i = {}^B\boldsymbol{R}_i \begin{bmatrix} 0 \\ 0 \\ 1 \end{bmatrix} = \begin{bmatrix} c\kappa_i s\psi_i \\ s\kappa_i s\psi_i \\ c\psi_i \end{bmatrix} = \begin{bmatrix} k_{xi} \\ k_{yi} \\ k_{zi} \end{bmatrix} \tag{5}$$

At the same time, the relationship between κ_i and ψ_i can be calculated as

$$\begin{aligned} c\psi_i &= k_{zi}; \\ s\psi_i &= \sqrt{k_{xi}^2 + k_{yi}^2}, \quad (0 \le \psi_i \le \pi); \\ s\kappa_i &= \frac{k_{yi}}{s\psi_i}; \\ c\kappa_i &= \frac{k_{xi}}{s\psi_i}; \end{aligned} \tag{6}$$

Substituting (4) and (5) into (3) and squaring both sides of (3) can be deduced as

$$s_{ai} s_i^2 + s_{bi} s_i + s_{ci} = 0 \tag{7}$$

where

$$\begin{aligned} s_{ai} &= B_{xi}^2 + B_{yi}^2 + B_{zi}^2; \\ s_{bi} &= 2\left(A_{xi}B_{xi} + A_{yi}B_{yi} + A_{zi}B_{zi}\right); \\ s_{ci} &= A_{xi}^2 + A_{yi}^2 + A_{zi}^2 - l_i^2; \\ A_{xi} &= R_m c\phi_i c\beta + R_m s\phi_i s\beta s\alpha - \left(R_b + d_1\right) c\varphi_i; \\ B_{xi} &= 0; \\ A_{yi} &= R_m s\phi_i c\alpha - \left(R_b + d_1\right) s\varphi_i; \\ B_{yi} &= 0; \\ A_{zi} &= z_m + R_m s\phi_i c\beta s\alpha - R_m c\phi_i s\beta; \\ B_{zi} &= -1; \end{aligned} \tag{8}$$

The inverse kinematics solutions for the ith limb can be derived from (7):

$$s_i = \frac{-s_{bi} \pm \sqrt{s_{bi}^2 - 4 s_{ai} s_{ci}}}{2 s_{ai}} \tag{9}$$

From (9), there are two solutions for each driving joint; that is to say, there exist eight possible solutions for a given configuration. However, the three driving sliders are only allowed moving downward from point B_i. Therefore, only the negative symbol can satisfy the motion characteristics of the parallel perfusion manipulator.

3.2. Forward Kinematics. Forward kinematics for the 3PSS-PU mechanism is to solve the pose parameters (α, β, z_m) after knowing the driving parameters (s_1, s_2, s_3). For this problem, it can be obtained from (3) and (4), which can lead to the following formula:

$$\begin{aligned} l_i \boldsymbol{k}_i &= \begin{bmatrix} x_{li} \\ y_{li} \\ z_{li} \end{bmatrix} \\ &= \begin{bmatrix} R_m c\phi_i c\beta + R_m s\phi_i s\beta s\alpha - \left(R_b + d_1\right) c\varphi_i \\ R_m s\phi_i c\alpha - \left(R_b + d_1\right) s\varphi_i \\ z_m + R_m s\phi_i c\beta s\alpha - R_m c\phi_i s\beta - s_i \end{bmatrix} \end{aligned} \tag{10}$$

According to constraint of the length of the links N_iM_i, the restraint equation can be obtained:

$$x_{li}^2 + y_{li}^2 + z_{li}^2 = l_i^2 \tag{11}$$

To solve the forward kinematics problem, β and z_m can be represented by α. Therefore, (12) can be derived from (10) and (11):

$$\begin{aligned} &z_m^2 + \left(A_i c\beta + R_i s\beta + Q_i\right) z_m + \left(C_i c\beta + D_i s\beta + E_i\right) \\ &\quad = 0 \end{aligned} \tag{12}$$

where the coefficients $A_i, Q_i \sim E_i$ are functions of α:

$$\begin{aligned} A_i &= 2R_m s\phi_i s\alpha; \\ R_i &= -2R_m c\phi_i; \\ Q_i &= -2s_i; \end{aligned}$$

$$\begin{aligned}
C_i &= -2R_m c\phi_i c\varphi_i \left(R_b + d_1\right) - 2R_m s_i s\alpha s\phi_i; \\
D_i &= 2R_m s_i c\phi_i - 2R_m c\varphi_i s\alpha s\phi_i \left(R_b + d_1\right); \\
E_i &= \left(R_b + d_1\right)^2 + R_m^2 + s_i^2 - l_i^2 \\
&\quad - 2R_m c\alpha s\phi_i s\varphi_i \left(R_b + d_1\right);
\end{aligned} \tag{13}$$

Equation (12) also can be further simplified by subtracting one equation from another, which yields the following expression:

$$\left(A_{ij}z_m + C_{ij}\right)c\beta + \left(R_{ij}z_m + D_{ij}\right)s\beta + Q_{ij}z_m + E_{ij} = 0 \tag{14}$$

where $i \neq j$ and

$$\begin{aligned}
A_{ij} &= A_i - A_j; \\
R_{ij} &= R_i - R_j; \\
Q_{ij} &= Q_i - Q_j; \\
C_{ij} &= C_i - C_j; \\
D_{ij} &= D_i - D_j; \\
E_{ij} &= E_i - E_j;
\end{aligned} \tag{15}$$

Therefore, β can be obtained by z_m and α as

$$\begin{aligned}
c\beta &= -\frac{Fz_m^2 + Gz_m + H}{Iz_m^2 + Jz_m + K}; \\
s\beta &= -\frac{Lz_m^2 + Sz_m + T}{Iz_m^2 + Jz_m + K}
\end{aligned} \tag{16}$$

where the coefficients $F \sim K, X$ are functions of α, which are expressed as

$$\begin{aligned}
F &= R_{12}Q_{13} - Q_{12}R_{13}; \\
G &= D_{12}Q_{13} + R_{12}E_{13} - E_{12}R_{13} - Q_{12}D_{13}; \\
H &= D_{12}E_{13} - E_{12}D_{13}; \\
I &= R_{12}A_{13} - A_{12}R_{13}; \\
J &= D_{12}A_{13} + R_{12}C_{13} - C_{12}R_{13} - A_{12}D_{13}; \\
K &= D_{12}C_{13} - C_{12}D_{13}; \\
L &= Q_{12}A_{13} - A_{12}Q_{13}; \\
S &= E_{12}A_{13} + Q_{12}C_{13} - C_{12}Q_{13} - A_{12}E_{13}; \\
T &= E_{12}C_{13} - C_{12}E_{13};
\end{aligned} \tag{17}$$

Since $c^2\beta + s^2\beta = 1$, substituting (16) into this formula yields

$$U_4 z_m^4 + U_3 z_m^3 + U_2 z_m^2 + U_1 z_m + U_0 = 0 \tag{18}$$

where

$$\begin{aligned}
U_4 &= F^2 + L^2 - I^2; \\
U_3 &= 2\left(FG + LS - IJ\right); \\
U_2 &= G^2 + S^2 - J^2 + 2FH + 2LT - 2IK; \\
U_1 &= 2GH + 2ST - 2JK; \\
U_0 &= H^2 + T^2 - K^2;
\end{aligned} \tag{19}$$

Equation (12) consists of three independent equations, and two independent equations have been obtained as shown in (16). Substituting (16) into (12), another equation can be deduced. For instance, when $i = 1$, the equation is expressed as

$$W_3 z_m^3 + W_2 z_m^2 + W_1 z_m + W_0 = 0 \tag{20}$$

where

$$\begin{aligned}
W_3 &= A_1 F + R_1 L - Q_1 I; \\
W_2 &= A_1 G + C_1 F + R_1 S + D_1 L - Q_1 J - E_1 I; \\
W_1 &= A_1 H + C_1 G + R_1 T + D_1 S - Q_1 K - E_1 J; \\
W_0 &= C_1 H + D_1 T - E_1 K;
\end{aligned} \tag{21}$$

It can be seen that (18) and (20) have a common solution of z_m. By using Bezout's method [31], the following determinant should be satisfied:

$$\begin{vmatrix}
U_4 & U_3 & U_2 & U_1 & U_0 & 0 & 0 \\
0 & U_4 & U_3 & U_2 & U_1 & U_0 & 0 \\
0 & 0 & U_4 & U_3 & U_2 & U_1 & U_0 \\
W_3 & W_2 & W_1 & W_0 & 0 & 0 & 0 \\
0 & W_3 & W_2 & W_1 & W_0 & 0 & 0 \\
0 & 0 & W_3 & W_2 & W_1 & W_0 & 0 \\
0 & 0 & 0 & W_3 & W_2 & W_1 & W_0
\end{vmatrix} = 0 \tag{22}$$

Thus, (22) becomes an equation about α when the displacement s_i is known. Now that all the equations have been obtained, the method to solve the forward kinematics problem can be given as follows: (i) to calculate α from (22), (ii) to calculate z_m from (20), and (iii) to calculate β from (16).

For step (i), the sine and cosine components of α should be replaced by $t = \tan(\alpha/2)$. Based on the standard transformation expression, the equation $s\alpha = (1-t^2)/(1+t^2)$, $c\alpha = 2t/(1+t^2)$ can be obtained. Finally, (22) becomes a polynomial algebraic equation about the variable t. Then, according to (ii) and (iii), the forward kinematics problem can be solved.

3.3. Jacobian Matrix. Taking the derivative of (3) with respect to time leads to

$$\dot{s}_i \boldsymbol{n}_i + \boldsymbol{\omega}_i \times l_i \boldsymbol{k}_i = \boldsymbol{v}_m + \boldsymbol{\omega}_m \times \boldsymbol{r}_i \tag{23}$$

where $\boldsymbol{v}_m = [0, 0, \dot{z}_m]^{\mathrm{T}}$ and $\boldsymbol{\omega}_m = [\dot{\alpha}, \dot{\beta}, 0]^{\mathrm{T}}$ denote the linear and angular velocity vector of the hybrid perfusion platform in the fixed coordinate system B-$x_b y_b z_b$, respectively.

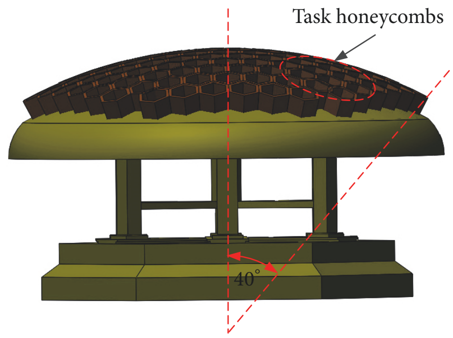

Figure 5: Structure of the spherical surface.

Taking the dot product with $\boldsymbol{k}_i$ on both sides of (23), the velocity of the ith driving joint can be deduced as

$$\dot{s}_i = \begin{bmatrix} \frac{\boldsymbol{k}_i^{\mathrm{T}}}{\boldsymbol{k}_i^{\mathrm{T}}\boldsymbol{n}_i} & \frac{(\boldsymbol{r}_i \times \boldsymbol{k}_i)^{\mathrm{T}}}{\boldsymbol{k}_i^{\mathrm{T}}\boldsymbol{n}_i} \end{bmatrix} \begin{bmatrix} \boldsymbol{v}_m \\ \boldsymbol{\omega}_m \end{bmatrix} = \boldsymbol{J}_i \begin{bmatrix} \boldsymbol{v}_m \\ \boldsymbol{\omega}_m \end{bmatrix} \tag{24}$$

Rewriting the velocities of the driving joints in the matrix form as

$$\dot{\boldsymbol{s}} = \boldsymbol{J}_s^{-1}\boldsymbol{J}_p\dot{\boldsymbol{P}} = \boldsymbol{J}\dot{\boldsymbol{P}} \tag{25}$$

where

$$\begin{aligned} \dot{\boldsymbol{s}} &= \begin{bmatrix} \dot{s}_1 & \dot{s}_2 & \dot{s}_3 \end{bmatrix}^{\mathrm{T}}; \\ \dot{\boldsymbol{P}} &= \begin{bmatrix} \boldsymbol{v}_m^{\mathrm{T}} & \boldsymbol{\omega}_m^{\mathrm{T}} \end{bmatrix}^{\mathrm{T}}; \\ \boldsymbol{J}_s &= \operatorname{diag}\left(\boldsymbol{k}_1^{\mathrm{T}}\boldsymbol{n}_1 \quad \boldsymbol{k}_2^{\mathrm{T}}\boldsymbol{n}_2 \quad \boldsymbol{k}_3^{\mathrm{T}}\boldsymbol{n}_3\right); \\ \boldsymbol{J}_p &= \begin{bmatrix} \boldsymbol{k}_1 & \boldsymbol{k}_2 & \boldsymbol{k}_3 \\ \boldsymbol{r}_1 \times \boldsymbol{k}_1 & \boldsymbol{r}_2 \times \boldsymbol{k}_2 & \boldsymbol{r}_3 \times \boldsymbol{k}_3 \end{bmatrix}^{\mathrm{T}}; \end{aligned} \tag{26}$$

The Jacobian matrix between the velocity vector $\dot{\boldsymbol{P}}$ and the driving joint velocity vector $\dot{\boldsymbol{s}}$ can be obtained as

$$\boldsymbol{J} = \boldsymbol{J}_s^{-1}\boldsymbol{J}_p = \begin{bmatrix} \boldsymbol{J}_1^{\mathrm{T}} & \boldsymbol{J}_2^{\mathrm{T}} & \boldsymbol{J}_3^{\mathrm{T}} \end{bmatrix}^{\mathrm{T}} \tag{27}$$

4. Kinematics Performance Analysis

Following the establishment of the mechanism model and the kinematics analysis, the analysis of the kinematics performance of the 3PSS-PU parallel manipulator will be conducted in this section, which includes the workspace, singularity, dexterity, and stiffness. The analysis of workspace is mainly on account of the kinematics solved in Section 3.1. And based on the Jacobian matrix analyzed in Section 3.3, the analyses of the singularity, dexterity, and stiffness are all developed in detail.

4.1. Workspace Analysis

4.1.1. Task Honeycombs Analysis. As shown in Figure 5, the maximum angle between the point on the spherical crown surface and the vertical axis is 40 degrees. Due to the large size of the spherical crown surface, it adopts the method of subarea perfusion to accomplish the perfusion of the large object, and the task honeycombs of subarea are shown in Figure 6. For the task honeycombs, the maximum angle $\theta_{\max}$ of the honeycombs is 10°. During the perfusion process and through the rotation of the spherical crown worktable and the movement of the parallel manipulator along the arc guide rail and the motion of the moving platform, the perfusion of all the honeycombs can be completed successfully.

4.1.2. Reachable Workspace Analysis. In this section, the reachable workspace of the perfusion manipulator is obtained by the method of the geometric constraints. As shown in Figure 7, the flow diagram for calculating the workspace of the perfusion manipulator has been given in detail. According to the flow diagram of the workspace and the parameters given in Table 1, the reachable workspace of the moving platform can be obtained.

As shown in Figures 8(a) and 8(b), the 3D view and vertical view of the reachable workspace for the parallel perfusion manipulator are obtained. From the 3D view of the workspace, it can be seen that the rotation range of the moving platform about x_b axis and y_b axis remains unchanged with the increase of the value of the variable z_m. For the task honeycombs of the subarea, the maximum angle of the task honeycombs is 10°, and then the task workspace can be described as the yellow region in Figure 8(b). From Figure 8(b), it also can be easily concluded that the task workspace is always within the reachable workspace of the parallel manipulator. That is to say, the proposed 1T2R parallel perfusion manipulator can complete the perfusion of the task honeycombs. Then, by the rotation of the spherical crown worktable and the movement of the parallel manipulator along the arc guide rail, the perfusion of all the honeycombs will be completed.

4.2. Singularity Analysis. The method based on the Jacobian matrices is the most common method to find the singularity of a mechanism [32]. In order to obtain all the singularity positions of the parallel manipulator, the determinant of the inverse Jacobian matrix $\boldsymbol{J}_s$ and forward Jacobian matrix $\boldsymbol{J}_p$ will be conducted. Based on the Jacobian matrix, the singularity conditions of the proposed parallel manipulator can be divided into three types, which include inverse kinematic singularity (IKS), direct kinematic singularity (DKS), and combined singularity (CS). And the conditions for satisfying these types of singularity can be given as follows:

$$\begin{aligned} &\text{IKS:}\ \det(\boldsymbol{J}_s) = 0,\ \det\left(\boldsymbol{J}_{ps}\right) \neq 0; \\ &\text{DKS:}\ \det(\boldsymbol{J}_s) \neq 0,\ \det\left(\boldsymbol{J}_{ps}\right) = 0; \\ &\text{CS:}\ \det(\boldsymbol{J}_s) = 0,\ \det\left(\boldsymbol{J}_{ps}\right) = 0; \end{aligned} \tag{28}$$

where $\boldsymbol{J}_{ps}$ is a 3×3 submatrix from $\boldsymbol{J}_p$.

As for the IKS singularity, it occurs when matrix $\boldsymbol{J}_s$ is not full rank, i.e., $\det(\boldsymbol{J}_s) = 0$ or $\boldsymbol{k}_i \cdot \boldsymbol{n}_i = 0$ $(i = 1, 2, 3)$, which means one or more PSS legs are perpendicular to their corresponding sliding rails. As shown in Figure 9, it

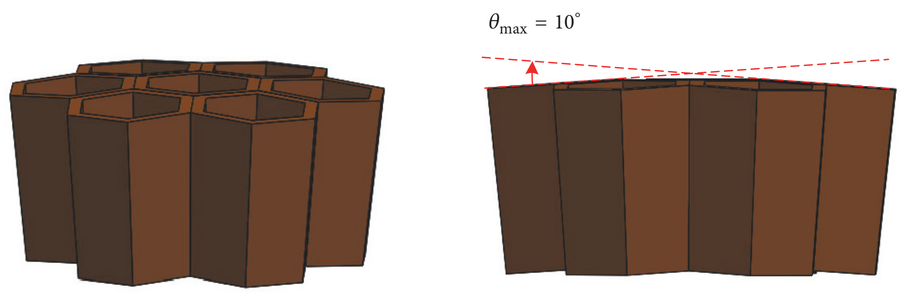

Figure 6: Task honeycombs of the subarea.

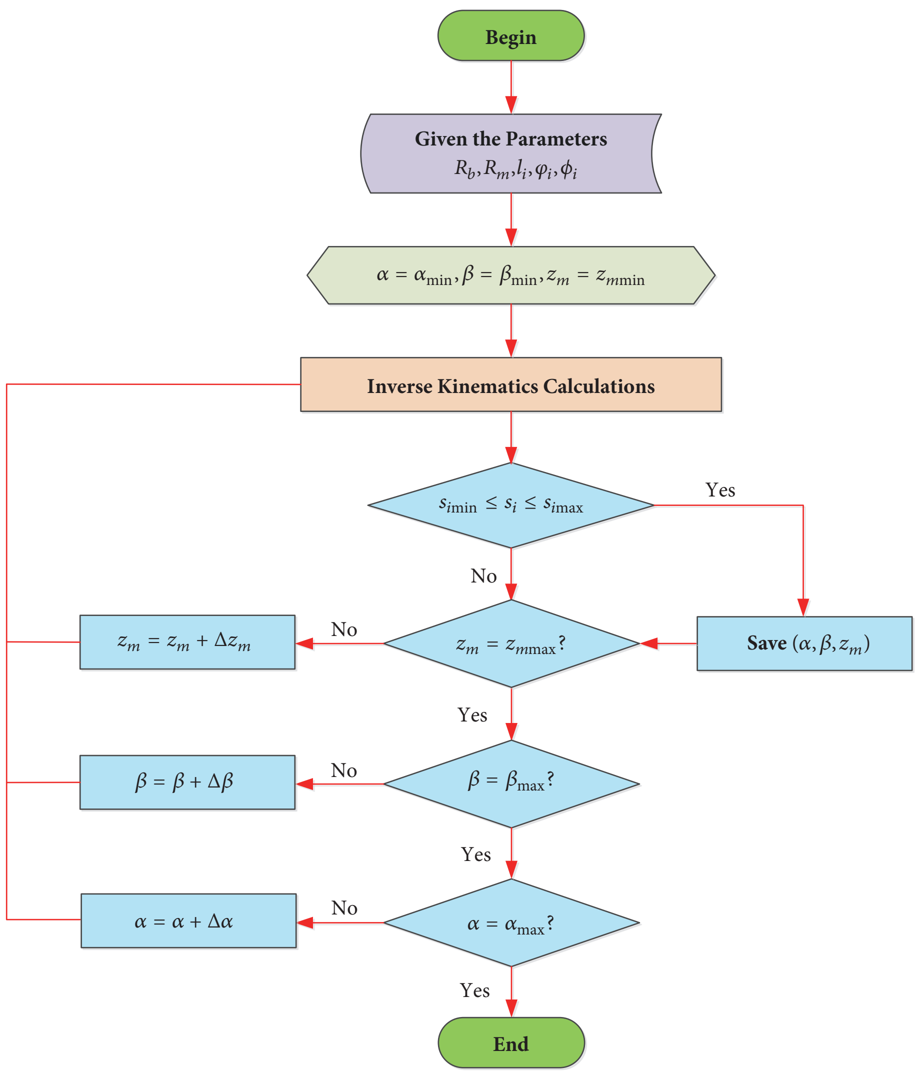

Figure 7: Flow chart for the reachable workspace.

Table 1: Dimensional parameters of 1T2R parallel manipulator.

Parameters	Values	Parameters	Values	Parameters	Values	Parameters	Values
R_b/mm	160	d_1/mm	50	α_{max}/rad	±0.6	z_{mmax}/mm	560
R_m/mm	270	s_{imin}/mm	0	β_{max}/rad	±0.6	φ_i/rad	$\pi/2 + 2\pi(i-1)/3$
l_i/mm	300	s_{imax}/mm	250	z_{mmin}/mm	300	ϕ_i/rad	$\pi/2 + 2\pi(i-1)/3$

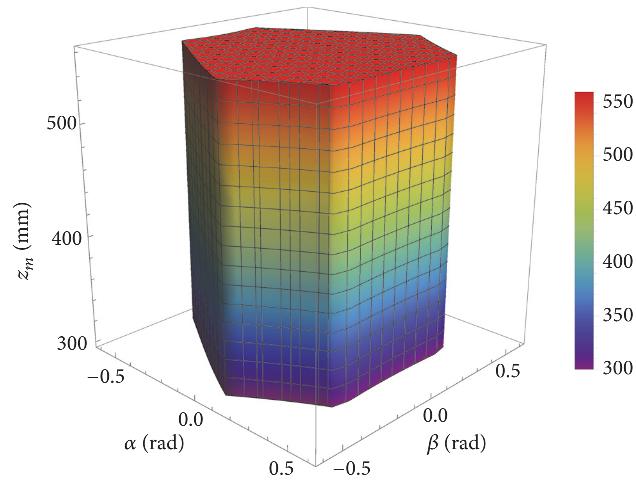

(a) 3D view of the reachable workspace

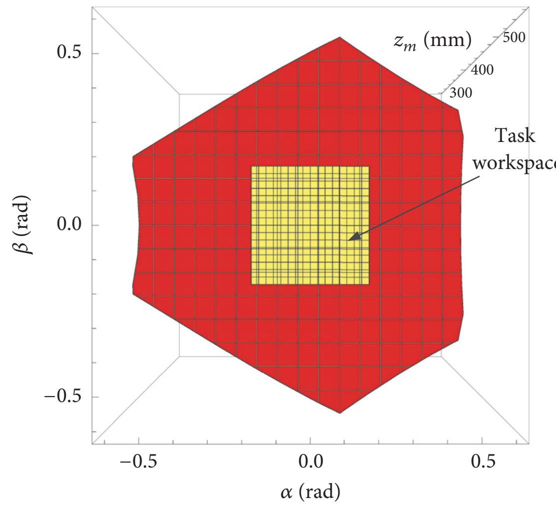

(b) Vertical view of the reachable workspace

Figure 8

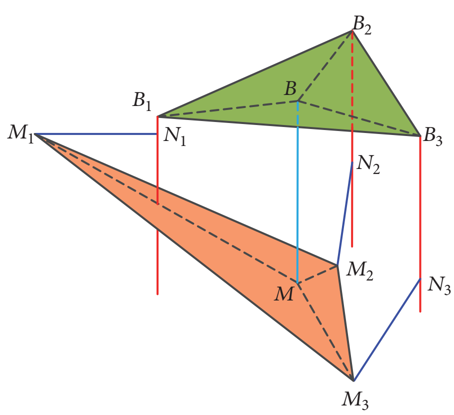

(a)

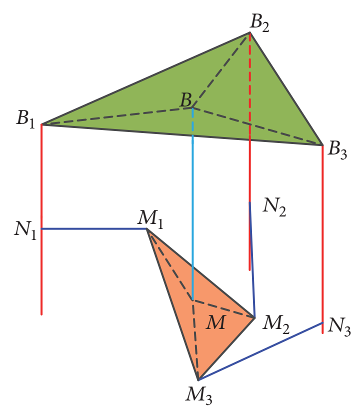

(b)

Figure 9: Manipulator positions when IKS happens.

gives two cases when the first link N_1M_1 is perpendicular to the corresponding sliding rails B_1N_1, and IKS occurs with $\det(\boldsymbol{J}_s) = 0$. In this case, the parallel manipulator loses one DoF because an infinitesimal motion of the actuator N_1 will cause no motion of the moving platform. From Figure 9(a), it can be seen that the interference between the moving platform and the sliding rail B_1N_1 occurs when the link N_1M_1 is perpendicular to the sliding rails B_1N_1 outside. Also, according to Figure 9(b), only when the size of the moving platform is smaller than the fixed platform can the inside vertical of the link N_1M_1 and the sliding rails B_1N_1 be satisfied. However, there is no interference between the components when the moving platform moves within its reachable workspace; thus the singularity case in Figure 9(a) is not exist. Also, for the proposed parallel manipulator, the parameter R_m is larger than R_b; thus the singularity case in Figure 9(b) does not exist either. Consequently, there is no IKS existing in the proposed parallel manipulator.

As for the DKS singularity, it occurs when matrix $\boldsymbol{J}_{ps}$ is not full rank; e.g., the first PSS branch lies in the plane $M_1M_2M_3$ with the link N_1M_1 passing through the center point M of the moving platform, which is shown in Figure 10. Under this situation, the moving platform obtains one more DoF even when all the three actuators are locked and the parallel manipulator will instantaneously be out of control; i.e., joint M_1 can infinitesimally move along the normal direction of the plane $M_1M_2M_3$ without actuation. From the first case in Figure 10(a), it can be known the interference between the moving platform and the sliding rail B_1N_1 occurs when the link N_1M_1 coincides with the line MM_1. Also, according to the singularity position in Figure 10(b), the link N_1M_1 is on the extension line of MM_1, and the size of the moving platform is smaller than the base platform. However, for the manipulator, there is no interference between the components when the moving platform moves within its reachable workspace, and the parameter R_m is larger than R_b. Consequently, there is no DKS existing in the parallel manipulator either.

Similarly, as for the CS singularity, it occurs when both of the matrices $\boldsymbol{J}_s$ and $\boldsymbol{J}_{ps}$ are not full rank. In this case, the

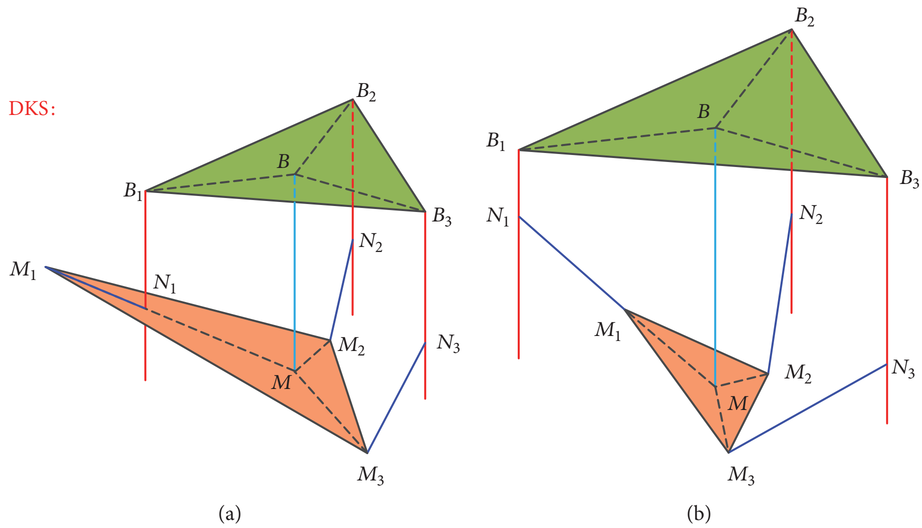

Figure 10: Manipulator positions when DKS happens.

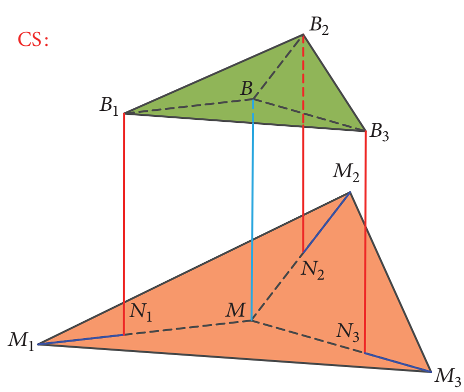

Figure 11: Manipulator position when CS happens.

inverse kinematic and forward kinematic singularities appear simultaneously, and the special singularity configuration is shown in Figure 11. According to Figure 11, it can be concluded that the combined singularity occurs when the relationship $R_m = R_b + l_i$ exists. However, the equation does not exist for the structure parameters of the proposed parallel manipulator. Therefore, there is no CS happening in the parallel manipulator either.

In summary, the three types of singularities mentioned above do not happen in the 3PSS-PU parallel manipulator because of the carefully designing structure parameters of the manipulator.

4.3. Dexterity and Stiffness Analysis. Dexterity and stiffness are important kinematic performance indexes to measure parallel manipulator's working ability. The dexterity mainly reflects the ability to arbitrarily change the moving platform's position and orientation or apply force and torques in arbitrary directions while working. And the stiffness directly affects manipulator's motion accuracy. Because the Jacobian matrix could reflect the relationship between input and output, the condition number of Jacobian matrix is frequently used in evaluating the dexterity of a manipulator. The calculation method of condition number comes out by computing the eigenvalue of stiffness matrix and taking square root of the ratio among extreme eigenvalues, which is shown in the following equation:

$$w_{con} = \frac{\sigma_{\max}}{\sigma_{\min}} \tag{29}$$

where w_{con} denotes the condition number of Jacobian matrix and $\sigma_{\max}$ and $\sigma_{\min}$ represent the maximum and minimum eigenvalues of stiffness matrix, respectively. And the stiffness matrix of the manipulator can be described as the following equation [33]:

$$\kappa(\boldsymbol{J}) = \boldsymbol{J}^{\mathrm{T}} \boldsymbol{K}_J \boldsymbol{J} \tag{30}$$

where $\boldsymbol{K}_J$ is the stiffness matrix and $\boldsymbol{K}_J = [\pi_1, \ldots \pi_2]$. In this paper, the actuators of the 3PSS-PU parallel manipulator can be seen as elastic components and π_i denotes the stiffness of the ith driving joint. Here, π_i is set to 100KN/m [7].

As shown in Figure 12, it describes the distributions of the Jacobian matrix condition number of the proposed parallel manipulator at a height of $z_m = 450$mm. From Figure 12, it can be seen that the values of condition number within the workspace all change from 5.2 to 9 smoothly. The closer the values of condition number to 1, the better the dexterity of the manipulator. The values of dexterity index for most areas of the workspace are all below 6.5, which indicate the good dexterity performance of the proposed parallel manipulator in the reachable workspace. Also, the dexterity performance is good enough to satisfy the dexterity requirements of the perfusion.

Meanwhile, the distributions of stiffness at different height of z_m are also plotted, which are shown in Figures 13 and 14. It can be easily observed from the figures that the stiffness of the manipulator decreases with the increasing of the value of z_m. And the distribution figures of stiffness with

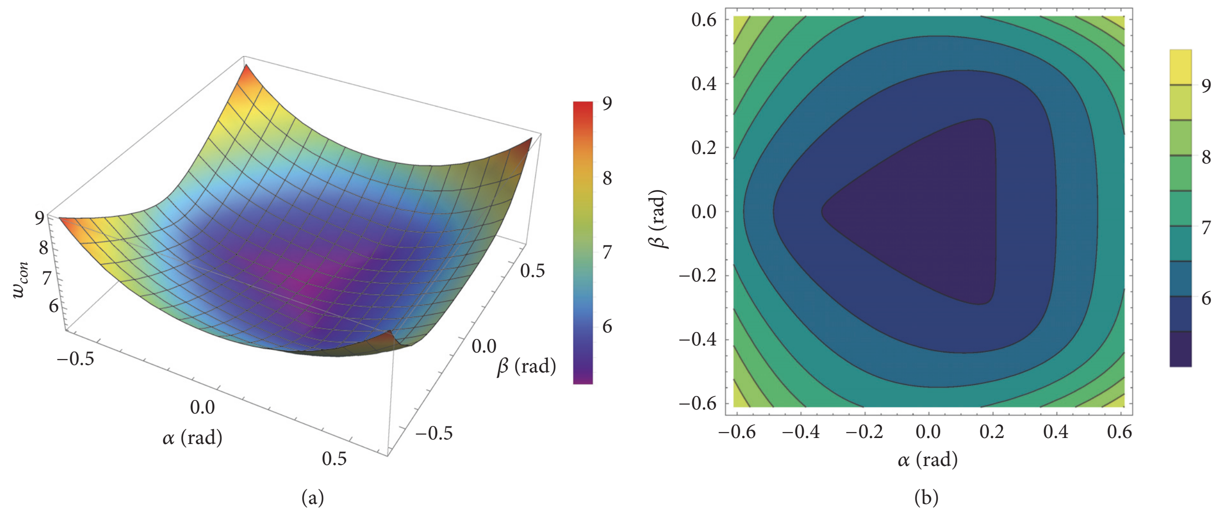

FIGURE 12: Distributions of condition number of Jacobian matrix at a height of z_m = 450mm.

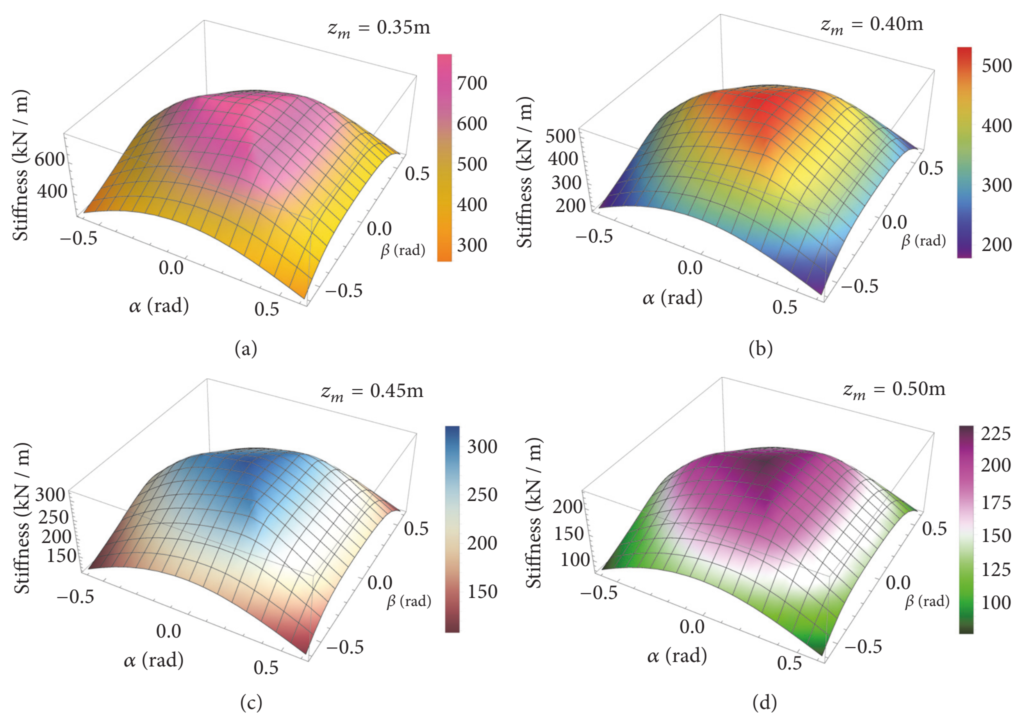

FIGURE 13: Distributions of stiffness at different height of z_m.

different value of z_m have the same change trend. Importantly, the maximum value of stiffness always arises at the center of the workspace and decreases with the angle α or β approaching to the maximum value, which is in line with the structural characteristics of the proposed parallel manipulator. Also, the value of the stiffness at different height of z_m is mostly above 150kN/m, and the stiffness requirement of the perfusion is about 100kN/m. Thus, the stiffness of the parallel manipulator is fully capable of satisfying the perfusion of the honeycombs.

5. Dynamics Model of the Parallel Manipulator

In this section, the dynamics analysis of the perfusion manipulator is mainly focused on the 1T2R parallel perfusion manipulator. Based on the principle of the virtual work [34, 35], the link Jacobian matrix and the dynamics model of the perfusion manipulator are established. The applied and inertia forces of the components are derived in the corresponding

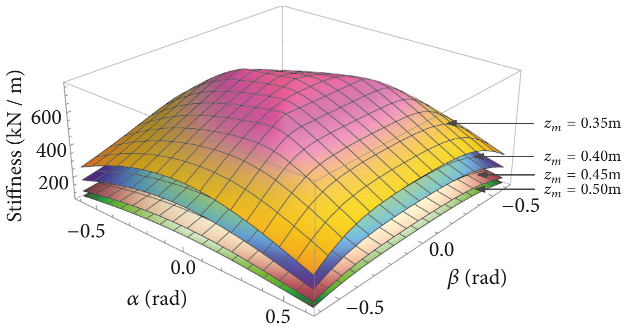

FIGURE 14: Comparison of stiffness at different height of z_m.

coordinate system. At last, the expression of the driving force is obtained.

5.1. Link Velocity Analysis. The velocity vector of the point M_i in the N_i-$x_i y_i z_i$ coordinate system can be written as

$$ {}^i\boldsymbol{v}_{Mi} = \dot{s}_i {}^i\boldsymbol{n}_i + {}^i\boldsymbol{\omega}_i \times l_i {}^i\boldsymbol{k}_i = {}^i\boldsymbol{v}_m + {}^i\boldsymbol{\omega}_m \times {}^i\boldsymbol{r}_i \quad (31) $$

Because of ${}^i\boldsymbol{\omega}_i^{\mathrm{T}} {}^i\boldsymbol{k}_i = 0$, taking the cross product with ${}^i\boldsymbol{k}_i$ on both sides of (31), the angular velocity of the limb N_iM_i in the N_i-$x_i y_i z_i$ coordinate system is derived as

$$ \begin{aligned} {}^i\boldsymbol{\omega}_i &= \frac{1}{l_i}\left({}^i\boldsymbol{k}_i \times {}^i\boldsymbol{v}_{Mi} - {}^i\boldsymbol{k}_i \times \dot{s}_i {}^i\boldsymbol{n}_i\right) \\ &= \frac{1}{l_i}\left[\boldsymbol{T}\left({}^i\boldsymbol{k}_i\right) {}^i\boldsymbol{v}_{Mi} - \boldsymbol{T}\left({}^i\boldsymbol{k}_i\right) \dot{s}_i {}^i\boldsymbol{n}_i\right] \end{aligned} \quad (32) $$

where

$$ \boldsymbol{T}\left({}^i\boldsymbol{k}_i\right) = \begin{bmatrix} 0 & -{}^ik_{iz} & {}^ik_{iy} \\ {}^ik_{iz} & 0 & -{}^ik_{ix} \\ -{}^ik_{iy} & {}^ik_{ix} & 0 \end{bmatrix} \quad (33) $$

Substituting (24) and (31) into (32) leads to

$$ \begin{aligned} {}^i\boldsymbol{\omega}_i = \frac{1}{l_i}\Bigg\{&\left[\boldsymbol{T}\left({}^i\boldsymbol{k}_i\right) {}^i\boldsymbol{R}_B \quad -\boldsymbol{T}\left({}^i\boldsymbol{k}_i\right)\boldsymbol{T}\left({}^i\boldsymbol{r}_i\right) {}^i\boldsymbol{R}_B\right] \\ &- \left({}^i\boldsymbol{k}_i \times {}^i\boldsymbol{n}_i\right)\left[\frac{\boldsymbol{k}_i^{\mathrm{T}}}{\boldsymbol{k}_i^{\mathrm{T}}\boldsymbol{n}_i} \quad \frac{\left(\boldsymbol{r}_i \times \boldsymbol{k}_i\right)^{\mathrm{T}}}{\boldsymbol{k}_i^{\mathrm{T}}\boldsymbol{n}_i}\right]\Bigg\}\dot{\boldsymbol{P}} = \boldsymbol{J}_{\omega i}\dot{\boldsymbol{P}} \end{aligned} \quad (34) $$

where

$$ \begin{aligned} &\boldsymbol{T}\left({}^i\boldsymbol{r}_i\right) = \begin{bmatrix} 0 & -{}^ir_{iz} & {}^ir_{iy} \\ {}^ir_{iz} & 0 & -{}^ir_{ix} \\ -{}^ir_{iy} & {}^ir_{ix} & 0 \end{bmatrix}; \\ &{}^i\boldsymbol{R}_B = {}^B\boldsymbol{R}_i^{-1} = {}^B\boldsymbol{R}_i^{\mathrm{T}}; \end{aligned} \quad (35) $$

With reference to (31) and (34), the linear velocity of the mass center of the branch N_iM_i in the N_i-$x_i y_i z_i$ coordinate system can be given as

$$ \begin{aligned} {}^i\boldsymbol{v}_i &= {}^i\boldsymbol{v}_{Mi} - {}^i\boldsymbol{\omega}_i \times \frac{l_i}{2} {}^i\boldsymbol{k}_i \\ &= \left\{\left[{}^i\boldsymbol{R}_B \quad -\boldsymbol{T}\left({}^i\boldsymbol{r}_i\right) {}^i\boldsymbol{R}_B\right] + \frac{l_i}{2}\boldsymbol{T}\left({}^i\boldsymbol{k}_i\right)\boldsymbol{J}_{\omega i}\right\}\dot{\boldsymbol{P}} = \boldsymbol{J}_{vi}\dot{\boldsymbol{P}} \end{aligned} \quad (36) $$

Rewriting the velocity vector of the ith branch N_iM_i in the matrix form yields

$$ \begin{bmatrix} {}^i\boldsymbol{v}_i \\ {}^i\boldsymbol{\omega}_i \end{bmatrix} = \begin{bmatrix} \boldsymbol{J}_{vi} \\ \boldsymbol{J}_{\omega i} \end{bmatrix}\dot{\boldsymbol{P}} = \boldsymbol{J}_{v\omega i}\dot{\boldsymbol{P}} \quad (37) $$

where $\boldsymbol{J}_{v\omega i}$ is the link Jacobian matrix which represents the mapping between the velocity vector of the moving platform in the fixed system B-$x_b y_b z_b$ and the velocity vector of the ith link in the N_i-$x_i y_i z_i$ coordinate system.

5.2. Acceleration Analysis. Taking the derivative of (23) with respect to time leads to

$$ \begin{aligned} &\ddot{s}_i\boldsymbol{n}_i + \dot{\boldsymbol{\omega}}_i \times l_i\boldsymbol{k}_i + \boldsymbol{\omega}_i \times \left(\boldsymbol{\omega}_i \times l_i\mathbf{k}_i\right) \\ &\quad = \dot{\boldsymbol{v}}_m + \dot{\boldsymbol{\omega}}_m \times \boldsymbol{r}_i + \boldsymbol{\omega}_m \times \left(\boldsymbol{\omega}_m \times \boldsymbol{r}_i\right) \end{aligned} \quad (38) $$

Taking the dot product with $\boldsymbol{k}_i$ on both sides of (38) and simplifying the equation, the acceleration of the ith slider can be obtained as

$$ \begin{aligned} \ddot{s}_i = \boldsymbol{J}_i\ddot{\boldsymbol{P}} + \frac{1}{\boldsymbol{k}_i^{\mathrm{T}}\boldsymbol{n}_i}&\left[\left(\boldsymbol{k}_i^{\mathrm{T}}\boldsymbol{\omega}_m\right)\left(\boldsymbol{r}_i^{\mathrm{T}}\boldsymbol{\omega}_m\right) - \left(\boldsymbol{k}_i^{\mathrm{T}}\boldsymbol{r}_i\right)\left|\boldsymbol{\omega}_m\right|^2\right. \\ &\left. + l_i\left|\boldsymbol{k}_i \times \boldsymbol{\omega}_i\right|^2\right] \end{aligned} \quad (39) $$

The matrix form of the accelerations of the driving sliders can be rewritten as

$$ \ddot{\boldsymbol{s}} = \boldsymbol{J}\ddot{\boldsymbol{P}} + \boldsymbol{\psi} \quad (40) $$

where

$$ \begin{aligned} &\ddot{\boldsymbol{s}} = \left[\ddot{s}_1 \quad \ddot{s}_2 \quad \ddot{s}_3\right]^{\mathrm{T}}; \\ &\ddot{\boldsymbol{P}} = \left[\dot{\boldsymbol{v}}_m^{\mathrm{T}} \quad \dot{\boldsymbol{\omega}}_m^{\mathrm{T}}\right]^{\mathrm{T}}; \\ &\boldsymbol{\psi} = \left[\psi_1 \quad \psi_2 \quad \psi_3\right]^{\mathrm{T}}; \\ &\psi_i = \frac{1}{\boldsymbol{k}_i^{\mathrm{T}}\boldsymbol{n}_i}\left[\left(\boldsymbol{k}_i^{\mathrm{T}}\boldsymbol{\omega}_m\right)\left(\boldsymbol{r}_i^{\mathrm{T}}\boldsymbol{\omega}_m\right) - \left(\boldsymbol{k}_i^{\mathrm{T}}\boldsymbol{r}_i\right)\left|\boldsymbol{\omega}_m\right|^2\right. \\ &\qquad \left. + l_i\left|\boldsymbol{k}_i \times \boldsymbol{\omega}_i\right|^2\right] \end{aligned} \quad (41) $$

5.3. Link Acceleration Analysis. Taking the derivative of (31) with respect to time in the N_i-$x_i y_i z_i$ coordinate system leads to

$$ \begin{aligned} &\ddot{s}_i {}^i\boldsymbol{n}_i + {}^i\dot{\boldsymbol{\omega}}_i \times l_i {}^i\boldsymbol{k}_i + {}^i\boldsymbol{\omega}_i \times \left({}^i\boldsymbol{\omega}_i \times l_i {}^i\boldsymbol{k}_i\right) \\ &\quad = {}^i\dot{\boldsymbol{v}}_m + {}^i\dot{\boldsymbol{\omega}}_m \times {}^i\boldsymbol{r}_i + {}^i\boldsymbol{\omega}_m \times \left({}^i\boldsymbol{\omega}_m \times {}^i\boldsymbol{r}_i\right) \end{aligned} \quad (42) $$

Taking the cross product of (42) with ${}^{i}\boldsymbol{k}_i$ on both sides, the angular acceleration of the ith link N_iM_i can be obtained as

$$
\begin{aligned}
{}^{i}\dot{\boldsymbol{\omega}}_i = \frac{1}{l_i}\Big\{ & {}^{i}\boldsymbol{k}_i \times {}^{i}\dot{\boldsymbol{v}}_m + {}^{i}\boldsymbol{k}_i \times \left({}^{i}\dot{\boldsymbol{\omega}}_m \times {}^{i}\boldsymbol{r}_i\right) - \left({}^{i}\boldsymbol{k}_i \times {}^{i}\boldsymbol{n}_i\right)\ddot{s}_i \\
& + {}^{i}\boldsymbol{k}_i \times \left[{}^{i}\boldsymbol{\omega}_m \times \left({}^{i}\boldsymbol{\omega}_m \times {}^{i}\boldsymbol{r}_i\right)\right] - {}^{i}\boldsymbol{k}_i \\
& \times \left[{}^{i}\boldsymbol{\omega}_i \times \left({}^{i}\boldsymbol{\omega}_i \times l_i{}^{i}\boldsymbol{k}_i\right)\right]\Big\}
\end{aligned}
\tag{43}
$$

Based on the derived acceleration in (39), (43) can be simplified as

$$
{}^{i}\dot{\boldsymbol{\omega}}_i = \boldsymbol{J}_{\omega i}\ddot{\boldsymbol{P}} + \boldsymbol{\lambda}_i \tag{44}
$$

where

$$
\begin{aligned}
\boldsymbol{\lambda}_i = \frac{1}{l_i}\Bigg\{ & -\frac{\left({}^{i}\boldsymbol{k}_i \times {}^{i}\boldsymbol{n}_i\right)}{\boldsymbol{k}_i^{\mathrm{T}}\boldsymbol{n}_i}\left[\left(\boldsymbol{k}_i^{\mathrm{T}}\boldsymbol{\omega}_m\right)\left(\boldsymbol{r}_i^{\mathrm{T}}\boldsymbol{\omega}_m\right)\right. \\
& \left. - \left(\boldsymbol{k}_i^{\mathrm{T}}\boldsymbol{r}_i\right)\left|\boldsymbol{\omega}_m\right|^2 + l_i\left|\boldsymbol{k}_i \times \boldsymbol{\omega}_i\right|^2\right] + \left({}^{i}\boldsymbol{\omega}_m^{\mathrm{T}}{}^{i}\boldsymbol{r}_i\right)\left({}^{i}\boldsymbol{k}_i\right. \\
& \left.\times {}^{i}\boldsymbol{\omega}_m\right) - \left|{}^{i}\boldsymbol{\omega}_m\right|^2\left({}^{i}\boldsymbol{k}_i \times {}^{i}\boldsymbol{r}_i\right)\Bigg\}
\end{aligned}
\tag{45}
$$

Taking the derivative of (36) with respect to time leads to

$$
\begin{aligned}
{}^{i}\dot{\boldsymbol{v}}_i &= {}^{i}\dot{\boldsymbol{v}}_{Mi} - {}^{i}\dot{\boldsymbol{\omega}}_i \times \frac{l_i}{2}{}^{i}\boldsymbol{k}_i - {}^{i}\boldsymbol{\omega}_i \times \left({}^{i}\boldsymbol{\omega}_i \times \frac{l_i}{2}{}^{i}\boldsymbol{k}_i\right) \\
&= {}^{i}\dot{\boldsymbol{v}}_m - \boldsymbol{T}\left({}^{i}\boldsymbol{r}_i\right){}^{i}\dot{\boldsymbol{\omega}}_m + \boldsymbol{T}\left({}^{i}\boldsymbol{\omega}_m\right)\boldsymbol{T}\left({}^{i}\boldsymbol{\omega}_m\right){}^{i}\boldsymbol{r}_i \\
&\quad + \frac{l_i}{2}\boldsymbol{T}\left({}^{i}\boldsymbol{k}_i\right){}^{i}\dot{\boldsymbol{\omega}}_i - \frac{l_i}{2}\boldsymbol{T}\left({}^{i}\boldsymbol{\omega}_i\right)\boldsymbol{T}\left({}^{i}\boldsymbol{\omega}_i\right){}^{i}\boldsymbol{k}_i
\end{aligned}
\tag{46}
$$

Substituting (44) into the above equation and simplifying can be derived as

$$
{}^{i}\dot{\boldsymbol{v}}_i = \boldsymbol{J}_{vi}\ddot{\boldsymbol{P}} + \boldsymbol{\eta}_i \tag{47}
$$

where $\boldsymbol{\eta}_i = \boldsymbol{T}({}^{i}\boldsymbol{\omega}_m)\boldsymbol{T}({}^{i}\boldsymbol{\omega}_m){}^{i}\boldsymbol{r}_i + (1/2)\boldsymbol{T}({}^{i}\boldsymbol{k}_i)\boldsymbol{\lambda}_i - (l_i/2)\boldsymbol{T}({}^{i}\boldsymbol{\omega}_i)\boldsymbol{T}({}^{i}\boldsymbol{\omega}_i){}^{i}\boldsymbol{k}_i$.

5.4. Dynamic Formulation. Applied and inertia forces imposed on the center of the mass of the moving perfusion platform can be derived as

$$
\mathbf{Q}_M = \begin{bmatrix} \boldsymbol{f}_e + m_m\boldsymbol{g} - m_m\dot{\boldsymbol{v}}_m \\ \boldsymbol{n}_e - {}^{B}\boldsymbol{I}_M\dot{\boldsymbol{\omega}}_m - \boldsymbol{\omega}_m \times \left({}^{B}\boldsymbol{I}_M\boldsymbol{\omega}_m\right) \end{bmatrix} \tag{48}
$$

where $\boldsymbol{f}_e$ and $\boldsymbol{n}_e$ represent the external force and torque imposed on the mass center of the moving perfusion platform, m_m is the mass of the moving perfusion platform, and $\boldsymbol{g} = [0, 0, 9.8]^{\mathrm{T}} m/s^2$ is the gravity. ${}^{B}\boldsymbol{I}_M = {}^{B}\boldsymbol{R}_M\boldsymbol{I}_M{}^{M}\boldsymbol{R}_B$, and $\boldsymbol{I}_M$ denotes the inertia matrix of the moving perfusion platform about the mass center which is described in the M-$x_my_mz_m$ coordinate system.

The force system $\mathbf{Q}_M$ in (48) can be divided into four sections: the acceleration term $\mathbf{Q}_{MA}$, the velocity term $\mathbf{Q}_{MV}$, the gravity term $\mathbf{Q}_{MG}$, and the external force term $\mathbf{Q}_{ME}$, which can be listed as follows:

$$
\begin{aligned}
\mathbf{Q}_M &= \begin{bmatrix} -m_m\dot{\boldsymbol{v}}_m \\ -{}^{B}\boldsymbol{I}_M\dot{\boldsymbol{\omega}}_m \end{bmatrix} + \begin{bmatrix} \mathbf{0}_{1\times 3} \\ -\boldsymbol{\omega}_m \times \left({}^{B}\boldsymbol{I}_M\boldsymbol{\omega}_m\right) \end{bmatrix} + \begin{bmatrix} m_m\boldsymbol{g} \\ \mathbf{0}_{1\times 3} \end{bmatrix} \\
&\quad + \begin{bmatrix} \boldsymbol{f}_e \\ \boldsymbol{n}_e \end{bmatrix} = \mathbf{Q}_{MA} + \mathbf{Q}_{MV} + \mathbf{Q}_{MG} + \mathbf{Q}_{ME}
\end{aligned}
\tag{49}
$$

The force system imposed on the center of the mass of the ith branch N_iM_i can be deduced in the N_i-$x_iy_iz_i$ coordinate system as

$$
{}^{i}\mathbf{Q}_i = \begin{bmatrix} m_i{}^{i}\boldsymbol{R}_B\boldsymbol{g} - m_i{}^{i}\dot{\boldsymbol{v}}_i \\ -{}^{i}\boldsymbol{I}_i{}^{i}\dot{\boldsymbol{\omega}}_i - {}^{i}\boldsymbol{\omega}_i \times \left({}^{i}\boldsymbol{I}_i{}^{i}\boldsymbol{\omega}_i\right) \end{bmatrix} \tag{50}
$$

where m_i is the mass of the link N_iM_i and ${}^{i}\boldsymbol{I}_i$ is the inertia matrix of the ith limb N_iM_i about the center of its mass which is expressed in the N_i-$x_iy_iz_i$ coordinate system.

Similarly, the force system ${}^{i}\boldsymbol{Q}_i$ of the ith branch N_iM_i also can be decomposed into three parts as

$$
\begin{aligned}
{}^{i}\mathbf{Q}_i &= \begin{bmatrix} -m_i\boldsymbol{J}_{vi}\ddot{\boldsymbol{P}} \\ -{}^{i}\boldsymbol{I}_i\boldsymbol{J}_{\omega i}\ddot{\boldsymbol{P}} \end{bmatrix} + \begin{bmatrix} -m_i\boldsymbol{\eta}_i \\ -{}^{i}\boldsymbol{I}_i\boldsymbol{\lambda}_i - {}^{i}\boldsymbol{\omega}_i \times \left({}^{i}\boldsymbol{I}_i{}^{i}\boldsymbol{\omega}_i\right) \end{bmatrix} \\
&\quad + \begin{bmatrix} m_i{}^{i}\boldsymbol{R}_B\boldsymbol{g} \\ \mathbf{0}_{1\times 3} \end{bmatrix} = {}^{i}\mathbf{Q}_{Ai} + {}^{i}\mathbf{Q}_{Vi} + {}^{i}\mathbf{Q}_{Gi}
\end{aligned}
\tag{51}
$$

For the driving joint, the force system exerted at the mass center of the slider can be derived in the B-$x_by_bz_b$ coordinate system as

$$
\begin{aligned}
\boldsymbol{F}_i &= m_{si}\boldsymbol{g} - m_{si}\ddot{\boldsymbol{s}}_i = -m_{si}\boldsymbol{n}_i\boldsymbol{J}_i\ddot{\boldsymbol{P}} - m_{si}\psi_i\boldsymbol{n}_i + m_{si}\boldsymbol{g} \\
&= \boldsymbol{F}_{Ai} + \boldsymbol{F}_{Vi} + \boldsymbol{F}_{Gi}
\end{aligned}
\tag{52}
$$

where $\boldsymbol{F}_{Ai}$, $\boldsymbol{F}_{Vi}$, and $\boldsymbol{F}_{Gi}$ are the acceleration term, the velocity term, and the gravity term of the force system $\boldsymbol{F}_i$, respectively, and m_{si} is the mass of the ith slider.

For the middle passive link, the branch only can move along z_b axis. Thus, the force imposed on the center of the mass of the middle limb can be deduced in the B-$x_by_bz_b$ coordinate system as

$$
\begin{aligned}
\boldsymbol{F}_p &= -m_p\ddot{\boldsymbol{z}} + m_p\boldsymbol{g} = -m_p\boldsymbol{n}_0\boldsymbol{J}_0\ddot{\boldsymbol{P}} + m_p\boldsymbol{g} \\
&= \boldsymbol{F}_{Ap} + \boldsymbol{F}_{Gp}
\end{aligned}
\tag{53}
$$

where m_p is the mass of the passive link and $\boldsymbol{F}_{Ap}$ and $\boldsymbol{F}_{Gp}$ are the acceleration term and the gravity term of the force system $\boldsymbol{F}_p$, respectively. And $\ddot{\boldsymbol{z}} = \boldsymbol{n}_0\boldsymbol{J}_0\ddot{\boldsymbol{P}} = \begin{bmatrix} 0 & 0 & \ddot{z}_m \end{bmatrix}^{\mathrm{T}}$; $\boldsymbol{n}_0 = \begin{bmatrix} 0 & 0 & 1 \end{bmatrix}^{\mathrm{T}}$; $\boldsymbol{J}_0 = \begin{bmatrix} 0 & 0 & 1 & 0 & 0 & 0 \end{bmatrix}$.

Suppose the moving perfusion platform has a virtual displacement in the reachable workspace of the 1T2R parallel manipulator. Thus, based on the principle of the virtual work, the dynamics equation of the proposed manipulator can be obtained as follows:

$$\delta \boldsymbol{P}^{\mathrm{T}} \mathbf{Q}_M + \sum_{i=1}^{3} (\boldsymbol{n}_i \delta s_i)^{\mathrm{T}} \boldsymbol{F}_i + \sum_{i=1}^{3} \delta^i \boldsymbol{x}_i^{\mathrm{T}\,i} \mathbf{Q}_i + (\boldsymbol{n}_0 \delta z)^{\mathrm{T}} \boldsymbol{F}_p + \delta \boldsymbol{s}^{\mathrm{T}} \boldsymbol{f} = 0 \quad (54)$$

where $\boldsymbol{f} = [f_1 \quad f_2 \quad f_3]^{\mathrm{T}}$ is the driving forces of the sliders of the 1T2R parallel manipulator, $\delta \boldsymbol{P}$ and δs_i denote the virtual displacements of the moving platform and the ith driving slider, respectively, and $\delta^i \boldsymbol{x}_i$ is the virtual displacement of the ith limb $N_i M_i$ descripted in the N_i-$x_i y_i z_i$ coordinate system.

According to the link Jacobian matrix analyzed in Section 5.1, the virtual displacements mentioned above can be represented by the virtual displacement of the moving perfusion platform $\delta \boldsymbol{P}$ as follows:

$$\begin{aligned} \delta s_i^{\mathrm{T}} &= (\boldsymbol{J}_i \delta \boldsymbol{P})^{\mathrm{T}} = \delta \boldsymbol{P}^{\mathrm{T}} \boldsymbol{J}_i^{\mathrm{T}}; \\ \delta^i \boldsymbol{x}_i^{\mathrm{T}} &= \delta \boldsymbol{P}^{\mathrm{T}} \boldsymbol{J}_{v\omega i}^{\mathrm{T}}; \\ \delta z^{\mathrm{T}} &= (\boldsymbol{J}_0 \delta \boldsymbol{P})^{\mathrm{T}} = \delta \boldsymbol{P}^{\mathrm{T}} \boldsymbol{J}_0^{\mathrm{T}}; \\ \delta \boldsymbol{s}^{T} &= \delta \boldsymbol{P}^{\mathrm{T}} \boldsymbol{J}^{\mathrm{T}} \end{aligned} \quad (55)$$

Substituting (55) into the dynamics equation leads to

$$\delta \boldsymbol{P}^{\mathrm{T}} \mathbf{Q}_M + \sum_{i=1}^{3} \delta \boldsymbol{P}^{\mathrm{T}} \boldsymbol{J}_i^{\mathrm{T}} \boldsymbol{n}_i^{\mathrm{T}} \boldsymbol{F}_i + \sum_{i=1}^{3} \delta \boldsymbol{P}^{\mathrm{T}} \boldsymbol{J}_{v\omega i}^{\mathrm{T}}\, {}^i\mathbf{Q}_i + \delta \boldsymbol{P}^{\mathrm{T}} \boldsymbol{J}_0^{\mathrm{T}} \boldsymbol{n}_0^{\mathrm{T}} \boldsymbol{F}_p + \delta \boldsymbol{P}^{\mathrm{T}} \boldsymbol{J}^{\mathrm{T}} \boldsymbol{f} = 0 \quad (56)$$

Simplifying (56), the inverse dynamics of the 1T2R parallel manipulator can be derived as follows:

$$\begin{aligned} \boldsymbol{f} &= -\boldsymbol{J}^{-\mathrm{T}} \left[\mathbf{Q}_M + \sum_{i=1}^{3} \left(\boldsymbol{J}_i^{\mathrm{T}} \boldsymbol{n}_i^{\mathrm{T}} \boldsymbol{F}_i + \boldsymbol{J}_{v\omega i}^{\mathrm{T}}\, {}^i\mathbf{Q}_i \right) + \boldsymbol{J}_0^{\mathrm{T}} \boldsymbol{n}_0^{\mathrm{T}} \boldsymbol{F}_p \right] \\ &= -\boldsymbol{J}^{-\mathrm{T}} \left[\sum_{i=1}^{3} \left(\boldsymbol{J}_i^{\mathrm{T}} \boldsymbol{n}_i^{\mathrm{T}} \boldsymbol{F}_{Ai} + \boldsymbol{J}_{v\omega i}^{\mathrm{T}}\, {}^i\mathbf{Q}_{Ai} \right) + \boldsymbol{J}_0^{\mathrm{T}} \boldsymbol{n}_0^{\mathrm{T}} \boldsymbol{F}_{Ap} + \mathbf{Q}_{MA} \right] - \boldsymbol{J}^{-\mathrm{T}} \left[\sum_{i=1}^{3} \left(\boldsymbol{J}_i^{\mathrm{T}} \boldsymbol{n}_i^{\mathrm{T}} \boldsymbol{F}_{Vi} + \boldsymbol{J}_{v\omega i}^{\mathrm{T}}\, {}^i\mathbf{Q}_{Vi} \right) + \mathbf{Q}_{MV} \right] \\ &\quad - \boldsymbol{J}^{-\mathrm{T}} \left[\sum_{i=1}^{3} \left(\boldsymbol{J}_i^{\mathrm{T}} \boldsymbol{n}_i^{\mathrm{T}} \boldsymbol{F}_{Gi} + \boldsymbol{J}_{v\omega i}^{\mathrm{T}}\, {}^i\mathbf{Q}_{Gi} \right) + \boldsymbol{J}_0^{\mathrm{T}} \boldsymbol{n}_0^{\mathrm{T}} \boldsymbol{F}_{Gp} + \mathbf{Q}_{MG} \right] - \boldsymbol{J}^{-\mathrm{T}} \mathbf{Q}_{ME} \end{aligned} \quad (57)$$

where $\boldsymbol{J}^{-\mathrm{T}}$ are the inverse matrix of $\boldsymbol{J}^{\mathrm{T}}$.

6. Numerical Simulation

In order to verify the correctness of the kinematics and dynamics model of the parallel manipulator, the comparison of theoretical and simulation curves of the motion parameters for the sliders based on the Mathematica and Adams software is conducted in this section. Three kinds of rotational motions of the moving perfusion platform are selected as simulation motion trajectory to analysis the motion and driving force of the driving slider. In the initial position, the displacement of all the driving sliders is 130mm and the moving platform is parallel to the base platform. The mass parameters of the parallel manipulator are given in Table 2, and the inertia matrices used in the simulation are also given as follows:

Table 2: The mass parameters of the proposed 1T2R parallel manipulator (kg).

Parameters	m_{si}	m_i	m_p	m_m
Mass	2.0	3.0	3.0	7.5

$$\begin{aligned} \boldsymbol{I}_M &= \begin{bmatrix} 0.171 & 0 & 0 \\ 0 & 0.171 & 0 \\ 0 & 0 & 0.341 \end{bmatrix} \mathrm{kg} \cdot \mathrm{m}^2; \\ {}^i\boldsymbol{I}_i &= \begin{bmatrix} 0.031 & 0 & 0 \\ 0 & 0.031 & 0 \\ 0 & 0 & 0.0003 \end{bmatrix} \mathrm{kg} \cdot \mathrm{m}^2; \end{aligned} \quad (58)$$

The external force and torque exerted on the moving perfusion platform can be given as follows:

$$\begin{aligned} \boldsymbol{f}_e &= (30.0, \ -20.0, \ 25.0)^{\mathrm{T}} \\ \boldsymbol{n}_e &= (0.0, \ -25.0, \ 0.0)^{\mathrm{T}} \end{aligned} \quad (59)$$

For the first kind of rotational motion, a pure rotation about x_b axis from 0 to -0.3rad is given without the translational motion of the moving platform, and the rotational motion of the moving platform can be described as

$$\alpha = -0.3 \left[35 \left(\frac{t}{4} \right)^4 - 84 \left(\frac{t}{4} \right)^5 + 70 \left(\frac{t}{4} \right)^6 - 20 \left(\frac{t}{4} \right)^7 \right] \quad (60)$$

As shown in Figure 15, the simplified simulation model in Adams is given, and the curves of driving forces in Adams are also shown. Based on the simulation curves, the points of different motion parameters can be extracted. Then, by utilizing the Mathematica software, the comparison curves of the displacement, velocity, acceleration, and driving force of the sliders are illustrated in Figures 16 and 17, respectively. In each figure, the black solid curves are the theoretical curves of the motion parameters of the driving sliders calculated by Mathematica software, and the red, green, and blue dashed curves are the simulation curves of the first, the second, and the third driving sliders' motion parameters obtained from the Adams software, respectively. Also, the motion parameters of different driving sliders are marked by characters "m", "n", and "o", respectively. For the driving

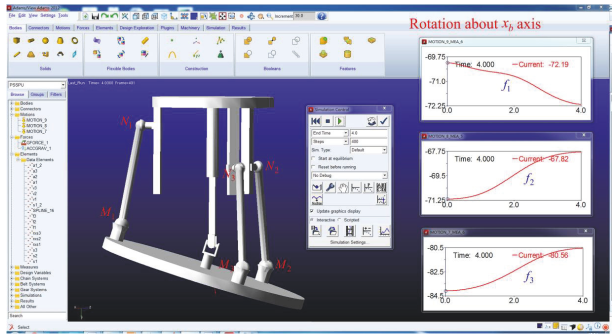

Figure 15: The simplified simulation model of rotation about x_b axis in Adams.

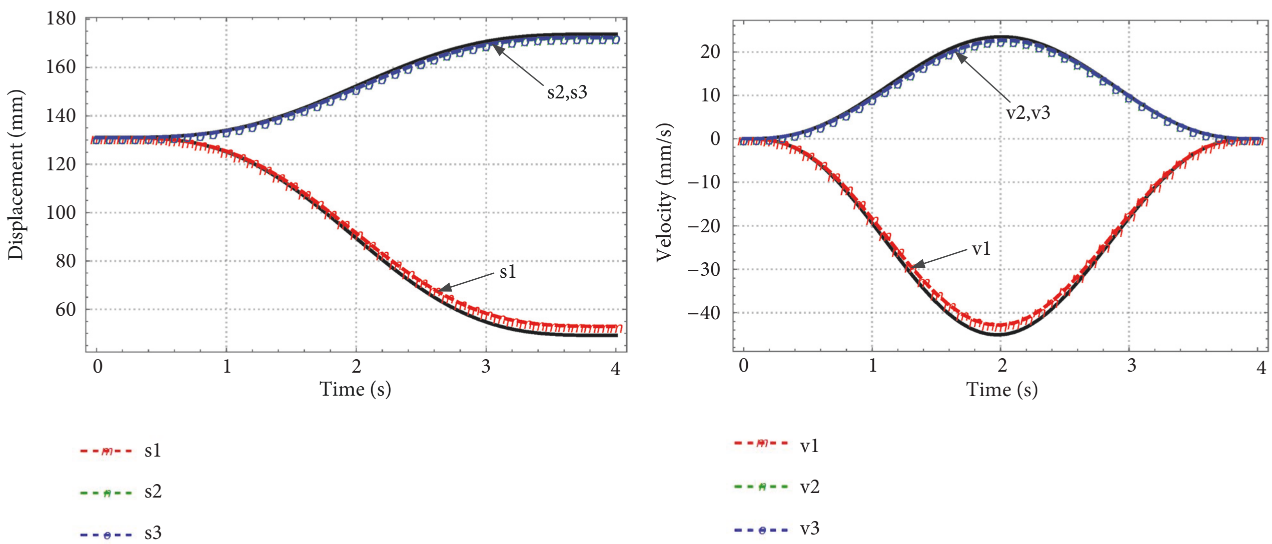

(a)

(b)

Figure 16: The comparison curves of the displacement and the velocity for the driving sliders under the rotation about x_b axis.

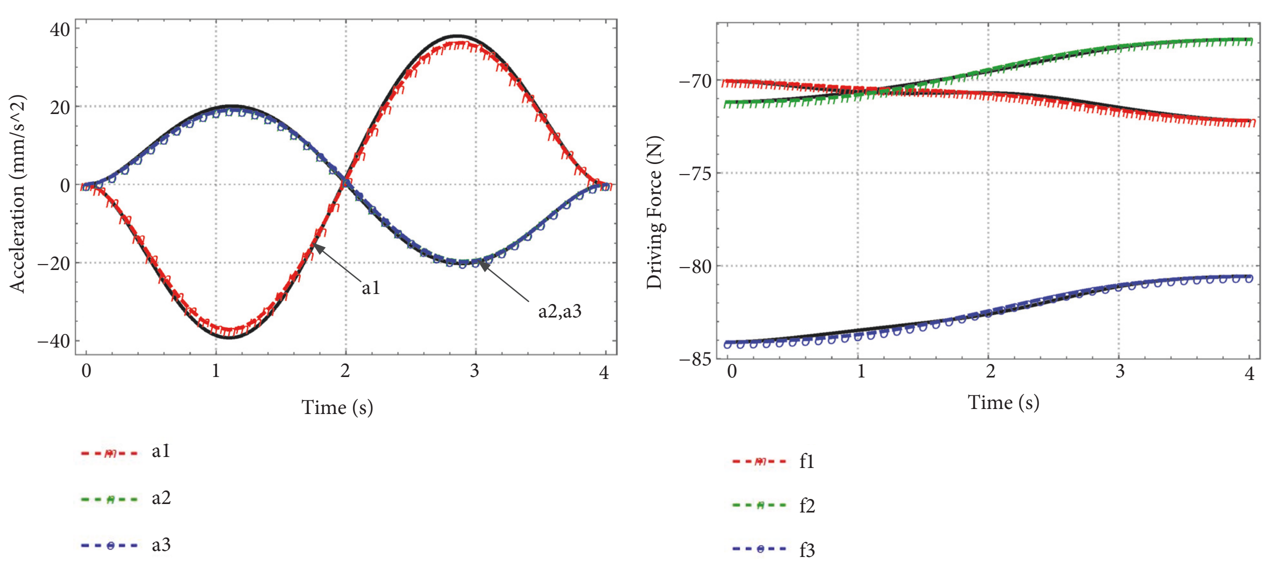

(a)

(b)

Figure 17: The comparison curves of the acceleration and the driving force for the driving sliders under the rotation about x_b axis.

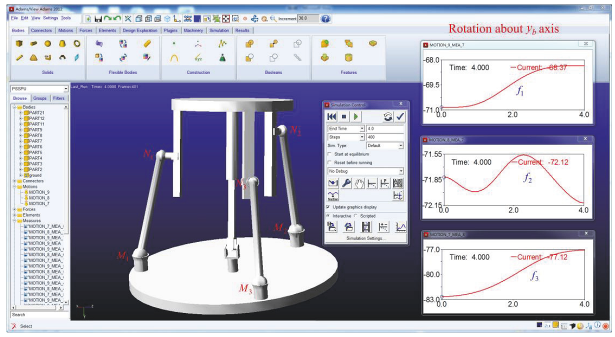

Figure 18: The simplified simulation model of rotation about y_b axis in Adams.

force in Figure 17, the negative sign indicates the opposite direction along the z_b axis.

According to these figures, it can be concluded that the theoretical and simulation curves of the motion parameters for the driving joints have the same change trend, respectively. And the curves of motion parameter change smoothly and continuously, which indicates the parallel manipulator has a good performance along the rotation about x_b axis. For the passive PU link, one of the rotation axes of the U joint connected to the moving platform has the same direction as the axis y_b. Thus, according to the symmetry of the mechanism, when the moving platform rotates around the x_b axis, the second and the third driving joints should have the same motion trajectory. Obviously, the displacement, velocity, and acceleration curves of the second and the third driving sliders in the simulation curves are all the same, respectively, which verifies the correctness of the establishment of kinematics model again.

For the second and third kinds of rotational motions, a pure rotation about y_b axis from 0 to -0.3rad and a simultaneous rotation about x_b axis and y_b axis from 0 to -0.3rad are given, respectively. Then the two kinds of rotational motions can be described, respectively, as follows:

$$\beta = -0.3\left[35\left(\frac{t}{4}\right)^4 - 84\left(\frac{t}{4}\right)^5 + 70\left(\frac{t}{4}\right)^6 - 20\left(\frac{t}{4}\right)^7\right] \quad (61)$$

$$\begin{aligned}\alpha &= -0.3\left[35\left(\frac{t}{4}\right)^4 - 84\left(\frac{t}{4}\right)^5 + 70\left(\frac{t}{4}\right)^6 - 20\left(\frac{t}{4}\right)^7\right] \\ \beta &= -0.3\left[35\left(\frac{t}{4}\right)^4 - 84\left(\frac{t}{4}\right)^5 + 70\left(\frac{t}{4}\right)^6 - 20\left(\frac{t}{4}\right)^7\right]\end{aligned} \quad (62)$$

Similarly, the simplified simulation models of rotation about y_b axis and rotation about x_b and y_b axis in Adams are presented in Figures 18 and 21, respectively. Then, the comparison curves of the displacement, velocity, acceleration, and driving force of the sliders under the two kinds of rotational motions are obtained as shown in Figures 19, 20, 22, and 23, respectively. As mentioned above, the black solid curves and the red, green, and blue dashed curves also represent the theoretical and simulation curves, respectively. And the motion parameters of different driving sliders are also marked by characters "m", "n", and "o", respectively. It also can be concluded that the theoretical and simulation curves of the motion parameters for the sliders all have the same change trend, respectively. Moreover, from the smoothly change trend of the motion curves, the good rotation performance of the parallel manipulator is proved again.

In summary, through the comparison of theoretical and simulation curves of the displacement, velocity, acceleration, and driving force for the sliders under the different rotational motions of the moving platform, the correctness of the kinematics and dynamics model of the parallel manipulator has been verified. Moreover, the good rotation performance of the proposed parallel manipulator is also proved. From the curves of the driving force, it can be concluded that the driving forces of the three driving sliders all vary from 68N to 85N, which indicates that all the driving joints are evenly stressed.

7. Conclusions

The main work and conclusions can be drawn as follows.

(1) In this paper, a novel hybrid perfusion system has been proposed, which is constructed by a 1T2R parallel perfusion manipulator and an arc guide way and can be used for the perfusion of the honeycombs in the thermal protection system of the spacecraft.

(2) The inverse kinematics and the Jacobian matrix are analyzed comprehensively. Then, based on the kinematics analysis, the performance analysis for the parallel manipulator is carried out. The analysis results show that the workspace and the stiffness of the proposed parallel manipulator all could satisfy the perfusion requirements and there is no singularity position within the workspace, which proved the good kinematics performance of the parallel manipulator.

(3) Through the analysis of the velocity and acceleration of the components, the dynamics model has been established by utilizing the principle of virtual work. According to the comparison of theoretical and simulation curves of the motion parameters for the sliders, the correctness of the kinematics and dynamics model of the parallel manipulator is verified. Also, the verified kinematics and dynamics models will provide a good theoretical foundation for the optimal

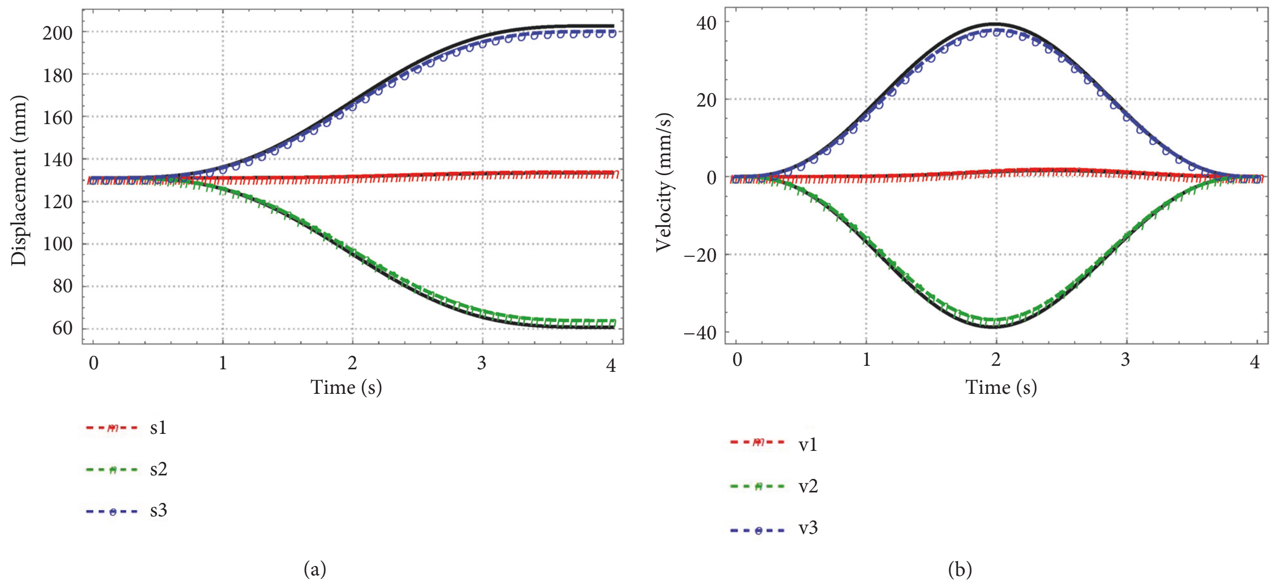

Figure 19: The comparison curves of the displacement and the velocity for the sliders under the rotation about y_b axis.

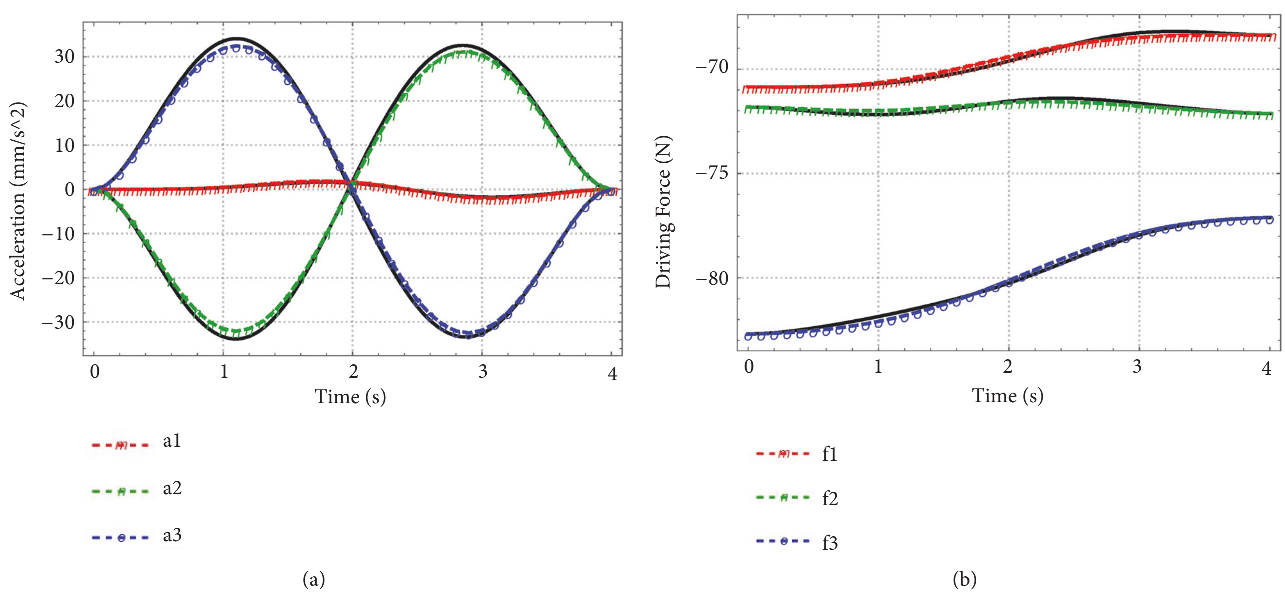

Figure 20: The comparison curves of the acceleration and the driving force for the sliders under the rotation about y_b axis.

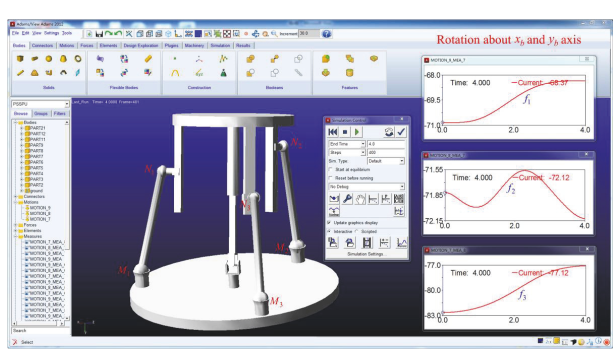

Figure 21: The simplified simulation model of rotation about x_b and y_b axis in Adams.

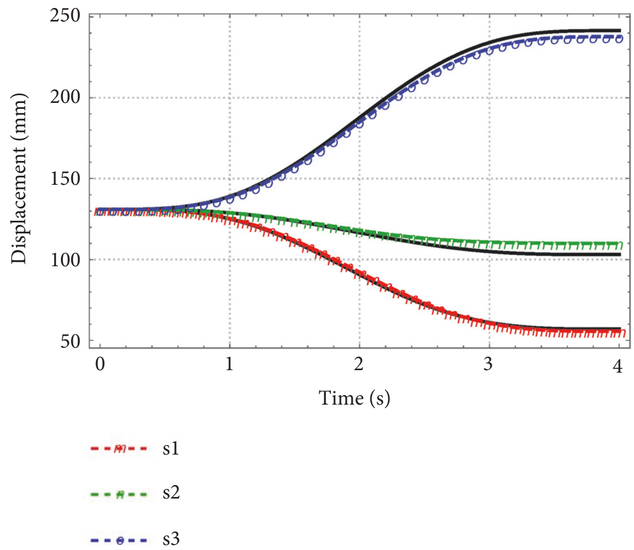

(a)

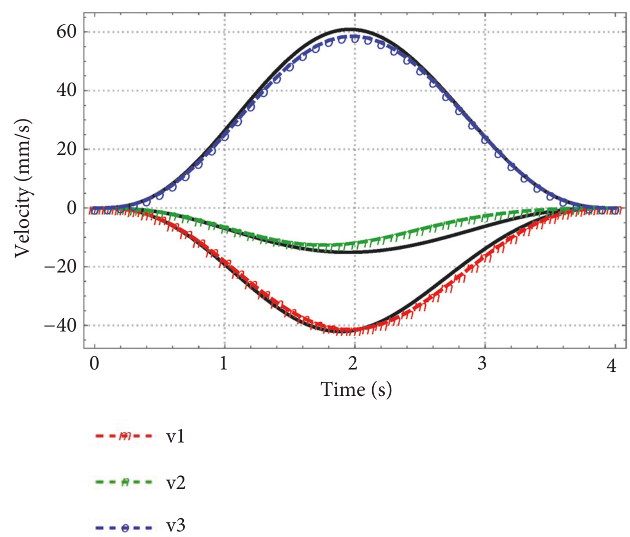

(b)

Figure 22: The comparison curves of the displacement and the velocity for the sliders under the rotation about x_b and y_b axis.

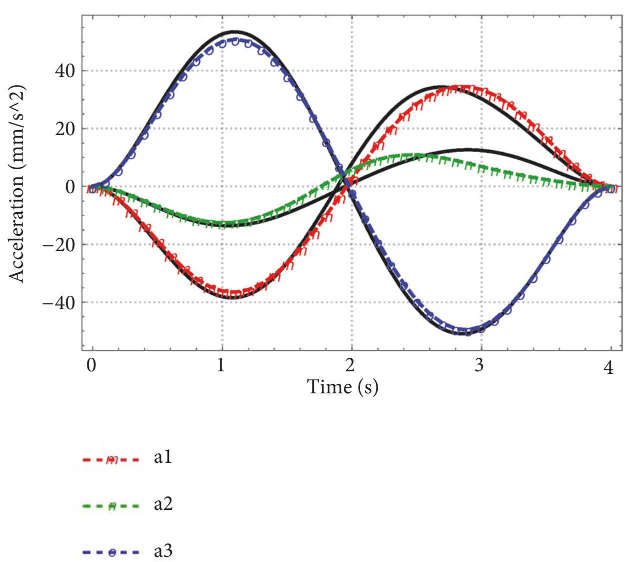

(a)

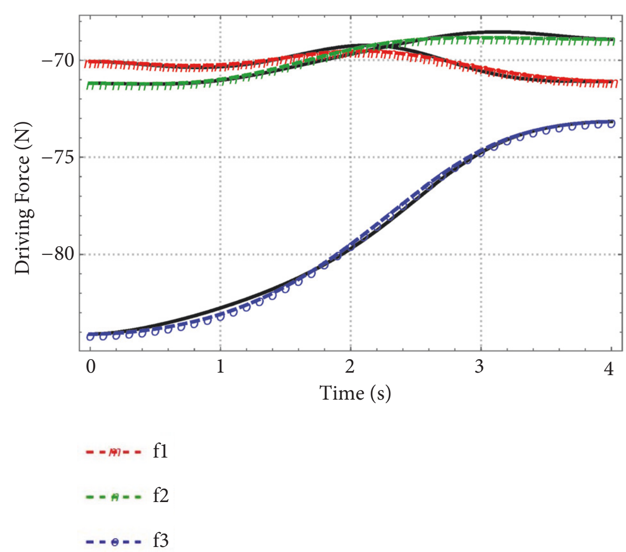

(b)

Figure 23: The comparison curves of the acceleration and the driving force for the sliders under the rotation about x_b and y_b axis.

design of the driving force and the research of the control strategy in the future research.

Data Availability

The data used to support the findings of this study are available from the corresponding author upon request.

Conflicts of Interest

The authors declare no potential conflicts of interest with respect to the research, authorship, and/or publication of this article.

Acknowledgments

The authors gratefully acknowledge the financial support of the Fundamental Research Funds for the Central Universities under Grant no. 2018JBZ007 and the National Natural Science Foundation of China (NSFC) under Grants 51675037 and 51505023.

References

[1] P. K. Ackerman, A. L. Baker, and C. W. Newquist, "Thermal protection system," Patent 5322725, US, 1994.

[2] C. Gogu, S. K. Bapanapalli, R. T. Haftka, and B. V. Sankar, "Comparison of materials for an integrated thermal protection

system for spacecraft reentry," *Journal of Spacecraft and Rockets*, vol. 46, no. 3, pp. 501–513, 2009.

[3] L. T. Chauvin, R. B. Erb, and D. H. Greenshields, "Apollo thermal-protection system development," *Journal of Spacecraft & Rockets*, vol. 7, pp. 839–869, 2015.

[4] D. Wu, A. Zhou, L. Zheng et al., "Study on the thermal protection performance of superalloy honeycomb panels in high-speed thermal shock environments," *Theoretical Applied Mechanics Letters*, vol. 4, no. 2, pp. 19–26, 2014.

[5] V. Murthy and K. J. Waldron, "Position kinematics of the generalized lobster arm and its series-parallel dual," *Journal of Mechanical Design*, vol. 114, no. 3, pp. 406–413, 1992.

[6] W. Ye, Y. Fang, and S. Guo, "Design and analysis of a reconfigurable parallel mechanism for multidirectional additive manufacturing," *Mechanism and Machine Theory*, vol. 112, pp. 307–326, 2017.

[7] X.-J. Liu, Z.-L. Jin, and F. Gao, "Optimum design of 3-DOF spherical parallel manipulators with respect to the conditioning and stiffness indices," *Mechanism and Machine Theory*, vol. 35, no. 9, pp. 1257–1267, 2000.

[8] C. Wang, Y. Fang, and S. Guo, "Design and Analysis of 3R2T and 3R3T Parallel Mechanisms With High Rotational Capability," *Journal of Mechanisms and Robotics*, vol. 8, no. 1, p. 011004, 2016.

[9] Y. Fang and L.-W. Tsai, "Structure synthesis of a class of 4-DoF and 5-DoF parallel manipulators with identical limb structures," *International Journal of Robotics Research*, vol. 21, no. 9, pp. 799–810, 2002.

[10] W. Dong, Z. Du, Y. Xiao, and X. Chen, "Development of a parallel kinematic motion simulator platform," *Mechatronics*, vol. 23, no. 1, pp. 154–161, 2013.

[11] B. Dasgupta and T. S. Mruthyunjaya, "The Stewart platform manipulator: a review," *Mechanism and Machine Theory*, vol. 35, no. 1, pp. 15–40, 2000.

[12] S. Guo, D. Li, H. Chen, and H. Qu, "Design and Kinematic Analysis of a Novel Flight Simulator Mechanism," in *Intelligent Robotics and Applications*, vol. 8917 of *Lecture Notes in Computer Science*, pp. 23–34, Springer International Publishing, Cham, 2014.

[13] Y. Xu, Y. Chen, G. Zhang, and P. Gu, "Adaptable design of machine tools structures," *Chinese Journal of Mechanical Engineering*, vol. 21, no. 3, pp. 7–15, 2008.

[14] Q. Li, L. Xu, Q. Chen, and W. Ye, "New Family of RPR-Equivalent Parallel Mechanisms: Design and Application," *Chinese Journal of Mechanical Engineering*, vol. 30, no. 2, pp. 217–221, 2017.

[15] J. Wu, J. Wang, L. Wang, T. Li, and Z. You, "Study on the stiffness of a 5-DOF hybrid machine tool with actuation redundancy," *Mechanism and Machine Theory*, vol. 44, no. 2, pp. 289–305, 2009.

[16] F. Xie, X. Liu, X. Luo, and M. Wabner, "Mobility, Singularity, and Kinematics Analyses of a Novel Spatial Parallel Mechanism," *Journal of Mechanisms and Robotics*, vol. 8, no. 6, p. 061022, 2016.

[17] F. Xie, X. Liu, J. Wang, and M. Wabner, "Kinematic Optimization of a Five Degrees-of-Freedom Spatial Parallel Mechanism With Large Orientational Workspace," *Journal of Mechanisms and Robotics*, vol. 9, no. 5, p. 051005, 2017.

[18] J. Mo, Z.-F. Shao, L. Guan, F. Xie, and X. Tang, "Dynamic performance analysis of the X4 high-speed pick-and-place parallel robot," *Robotics and Computer-Integrated Manufacturing*, vol. 46, pp. 48–57, 2017.

[19] L.-X. Xu and Y.-G. Li, "Investigation of joint clearance effects on the dynamic performance of a planar 2-DOF pick-and-place parallel manipulator," *Robotics and Computer-Integrated Manufacturing*, vol. 30, no. 1, pp. 62–73, 2014.

[20] G. Wu, S. Bai, and P. Hjørnet, "Architecture optimization of a parallel Schönflies-motion robot for pick-and-place applications in a predefined workspace," *Mechanism and Machine Theory*, vol. 106, pp. 148–165, 2016.

[21] F. Caccavale, B. Siciliano, and L. Villani, "The Tricept robot: dynamics and impedance control," *IEEE/ASME Transactions on Mechatronics*, vol. 8, no. 2, pp. 263–268, 2003.

[22] M. A. Hosseini, H.-R. M. Daniali, and H. D. Taghirad, "Dexterous workspace optimization of a Tricept parallel manipulator," *Advanced Robotics*, vol. 25, no. 13-14, pp. 1697–1712, 2011.

[23] H. Liu, T. Huang, J. Mei et al., "Kinematic design of a 5-DOF hybrid robot with large workspace/limb-stroke ratio," *Journal of Mechanical Design*, vol. 129, no. 5, pp. 530–537, 2007.

[24] T. Huang, M. Li, X. M. Zhao, J. P. Mei, D. G. Chetwynd, and S. J. Hu, "Conceptual design and dimensional synthesis for a 3-DOF module of the TriVariant - A novel 5-DOF reconfigurable hybrid robot," *IEEE Transactions on Robotics*, vol. 21, no. 3, pp. 449–456, 2005.

[25] Z. M. Bi and Y. Jin, "Kinematic modeling of Exechon parallel kinematic machine," *Robotics and Computer-Integrated Manufacturing*, vol. 27, no. 1, pp. 186–193, 2011.

[26] Z. M. Bi, "Kinetostatic modeling of Exechon parallel kinematic machine for stiffness analysis," *The International Journal of Advanced Manufacturing Technology*, vol. 71, no. 1-4, pp. 325–335, 2014.

[27] J. Wahl, "Articulated Tool Head. US," 6431802, 2002.

[28] X. Chen, X. Liu, F. Xie, and T. Sun, "A Comparison Study on Motion/Force Transmissibility of Two Typical 3-DOF Parallel Manipulators: The Sprint Z3 and A3 Tool Heads," *International Journal of Advanced Robotic Systems*, vol. 11, no. 1, p. 5, 2014.

[29] Y. Li, J. Wang, X.-J. Liu, and L.-P. Wang, "Dynamic performance comparison and counterweight optimization of two 3-DOF parallel manipulators for a new hybrid machine tool," *Mechanism and Machine Theory*, vol. 45, no. 11, pp. 1668–1680, 2010.

[30] D. Kanaan, P. Wenger, and D. Chablat, "Kinematic analysis of a serial–parallel machine tool: the VERNE machine," *Mechanism and Machine Theory*, vol. 44, no. 2, pp. 487–498, 2009.

[31] M. Shub and S. Smale, "Complexity of Bezout's theorem. IV: probability of success, extensions," *SIAM Journal on Numerical Analysis*, vol. 33, no. 1, pp. 128–148, 1996.

[32] G. Yang, S. H. Yeo, and C. B. Pham, "Kinematics and singularity analysis of a planar cable-driven parallel manipulator," in *Proceedings of the 2004 IEEE/RSJ International Conference on Intelligent Robots and Systems (IROS)*, pp. 3835–3840, Japan, October 2004.

[33] G. Coppola, D. Zhang, and K. Liu, "A 6-DOF reconfigurable hybrid parallel manipulator," *Robotics and Computer-Integrated Manufacturing*, vol. 30, no. 2, pp. 99–106, 2014.

[34] Y. Zhao and F. Gao, "Inverse dynamics of the 6-dof out-parallel manipulator by means of the principle of virtual work," *Robotica*, vol. 27, no. 2, pp. 259–268, 2009.

[35] B. Danaei, A. Arian, M. Tale Masouleh, and A. Kalhor, "Dynamic modeling and base inertial parameters determination of a 2-DOF spherical parallel mechanism," *Multibody System Dynamics*, vol. 41, no. 4, pp. 367–390, 2017.